Comput Mech (2016) 57:55–74
DOI 10.1007/s00466-015-1221-7

ORIGINAL PAPER

A two-scale generalized finite element method for fatigue crack propagation simulations utilizing a fixed, coarse hexahedral mesh

P. O'Hara[1] · J. Hollkamp[3] · C. A. Duarte[2] · T. Eason[3]

Received: 10 August 2015 / Accepted: 12 November 2015 / Published online: 24 November 2015

Abstract This paper presents a two-scale extension of the generalized finite element method (GFEM) which allows for static fracture analyses as well as fatigue crack propagation simulations on fixed, coarse hexahedral meshes. The approach is based on the use of specifically-tailored enrichment functions computed on-the-fly through the use of a fine-scale boundary value problem (BVP) defined in the neighborhood of existing mechanically-short cracks. The fine-scale BVP utilizes tetrahedral elements, and thus offers the potential for the use of a highly adapted fine-scale mesh in the regions of crack fronts capable of generating accurate enrichment functions for use in the coarse-scale hexahedral model. In this manner, automated *hp*-adaptivity which can be used for accurate fracture analyses, is now available for use on coarse, uniform hexahedral meshes without the requirements of irregular meshes and constrained approximations. The two-scale GFEM approach is verified and compared against alternative approaches for static fracture analyses, as well as mixed-mode fatigue crack propagation simulations. The numerical examples demonstrate the ability of the proposed approach to deliver accurate results even in scenarios involving multiple discontinuities or sharp kinks within a single computational element. The proposed approach is also applied to a representative panel model similar in design and complexity to that which may be used in the aerospace community.

Keywords Generalized finite elements · Multi-scale methods · Partition-of-unity methods · Computational fracture mechanics · hp-Methods

✉ P. O'Hara
patrick.ohara.ctr@wpafb.af.mil

[1] Universal Technology Corporation, 1270 North Fairfield Rd, Dayton, OH 45432, USA

[2] Newmark Laboratory, Department of Civil and Environmental Engineering, University of Illinois , 205 North Mathews Avenue, Urbana, IL 61801, USA

[3] Air Force Research Laboratory, Structural Sciences Center, WPAFB, Dayton, OH 45433, USA

1 Introduction

The physical phenomenon of fatigue crack propagation has been a relevant area of research in the civil, mechanical and aerospace communities for decades. There are many existing numerical techniques which are available to analyze such scenarios, with the generalized/extended finite element method (G/XFEM) [7,9,17,22,51,62] being one such technique, which has been actively developed over the past ten years or so. In contrast to standard finite element (FE) approaches in which the crack surface must 'fit' the FE mesh [59,66], the G/XFEM utilizes enrichment functions to accurately model the crack surface as it propagates throughout the computational domain, thus eliminating the potentially cumbersome meshing requirements associated with the standard FE approach. A potential limitation of the G/XFEM is the requirement of enrichment functions which can accurately model the physics of the problem at hand. Unfortunately, accurate closed-form enrichment functions are often unavailable, except for in a few specific cases. To meet the need of a more general enrichment function construction, the GFEM has been extended to the so-called GFEM with global-local enrichment functions (GFEM^{gl}) [16,33] in which an additional BVP is solved in a region of localized interest so as to numerically compute an appropriate enrichment function to model the relevant physics.

In this manner, the GFEM^{gl} is a more general form of the GFEM which does not require closed-form enrichment functions to be defined a priori, and it also represents a more truly multi-scale form of the GFEM which can enable the accurate and efficient modeling of localized features (in this instance cracks) which are significantly smaller than the size of the elements used to perform the numerical simulations. In order for the method to be more appropriate for the class of problems involving large, thin gauge panel-type structures, such as those commonly used in aerospace applications, the GFEM^{gl} has been formulated to incorporate the use of hexahedral elements for the fixed, coarse global discretization, while still allowing for the use of tetrahedral elements in the meshing of the highly adapted local domain.

The use of a 'small scale' BVP defined in a region of localized interest is not unique to the GFEM^{gl} approach. Other methods, such as the multi-scale FEM as proposed by Hou et al. [32], as well as the more recent variational multi-scale enrichment technique proposed by Oskay [47] also utilize the solutions of localized BVPs which are aimed at enhancing, or enriching the coarse-scale solution. Other multi-scale approaches which can be mentioned as potentially appropriate for the class of problems investigated in this work, while not necessarily taking the same approach as that proposed here; are the spectral overlay method of Belytschko et al. [8]; the superposition FEM (s-fem) of Fish and co-workers [20,21]; the combination s-fem/XFEM of Lee et al. [38]; the multi-scale FE approaches of Krause and co-workers [37,56], the multi-scale projection methods of Loehnert and co-workers [30,31,40] and the concurrent multi-level FE approaches proposed by Ghosh et el. [26,27].

A focus of the current work is on the ability of the GFEM^{gl} to accurately resolve local features (in this case cracks) which are smaller than the size of the elements used in the coarse-scale BVP, thus highlighting the multi-scale nature of the methodology. In particular, numerical examples are chosen to illustrate the ability of the approach to accurately represent sharp kinks, as well as multiple crack surfaces within a single element. The accurate representation of the crack surfaces themselves is done completely through enrichment, as no rigorous computational geometry engine [51] is available for hexahedral elements which would allow for the representation and potential evolution of the crack surfaces directly on a hexahedral mesh. It is worth noting that other global elements could be used, but it's likely that a more complicated integration scheme would be required (such as is presented in [20]) to integrate out the numerical enrichment functions if the local BVP is not properly nested within the global solid elements. This is not a problem with the use of global hexahedral elements, as this type of element allows for a straightforward conversion into nested tetrahedral elements [14].

The GFEM^{gl} using tetrahedral elements for both the global and local BVPs has been applied to linear elastic fracture mechanics (LEFM) analyses, as presented in detail by Kim et al. [33,53]. The suitability of the GFEM^{gl} with a global BVP composed of hexahedral elements has yet to be investigated. In this work we seek to illustrate the potential to extend the capability of the GFEM^{gl} to allow for automated *hp*-adaptivity to address LEFM problems analyzed using fixed, coarse hexahedral meshes. In general, *hp*-adaptivity is a non-trivial task on hexahedral meshes, and requires the use of irregular meshes, hanging nodes and constrained approximations [11,12]. The use of hanging nodes within the G/XFEM context has been investigated by Fries, et al. [23]. The approach proposed in this work, as will be demonstrated in detail, is able to circumvent this particular inconvenience, and still allow for the benefits of *hp*-adaptivity on a coarse, hexahedral mesh.

The remainder of the paper is structured as follows. A problem description with governing equations and a brief discussion of the crack propagation criteria used is presented next. Brief overviews of the GFEM and GFEM^{gl} are then presented, respectively. A series of numerical examples of increasing complexity are then provided to illustrate the potential of the proposed approach. Finally, the main conclusions from the current work are summarized.

2 Problem formulation

2.1 Governing equations

We consider a $3D$ domain, Ω, with external boundary $\partial\Omega$. Portions of $\partial\Omega$ are assumed to be subjected to (potentially cyclic) tractions and there is a pre-existing crack surface (potentially multiple) in the domain as illustrated in Fig. 1. We assume a linear elastic, homogeneous and isotropic material, thus yielding a typical LEFM scenario. We subdivide the external boundary into Γ^u and Γ^σ such that $\Gamma^u \cup \Gamma^\sigma = \partial\Omega$ and $\Gamma^u \cap \Gamma^\sigma = \emptyset$. Dirichlet and Neumann boundary conditions may then be prescribed on Γ^u and Γ^σ, respectively.

The equilibrium equations for the associated problem are

$$\nabla \cdot \boldsymbol{\sigma} + \boldsymbol{f}(\boldsymbol{x}) = 0 \tag{1}$$

where $\boldsymbol{\sigma}$ is the Cauchy stress tensor and $\boldsymbol{f}$ is the body force vector. Linear elastic material properties are assumed, leading to the following constitutive relations

$$\boldsymbol{\sigma}(\boldsymbol{x}) = \lambda tr\{\boldsymbol{\varepsilon}(\boldsymbol{x})\}\boldsymbol{I} + 2\mu\boldsymbol{\varepsilon}(\boldsymbol{x}) \tag{2}$$

where λ and μ are the two independent Lame elastic constants, $tr\{\boldsymbol{\varepsilon}\}$ is the trace of the small-strain tensor and $\boldsymbol{I}$ is the identity tensor. Making the additional assumption of

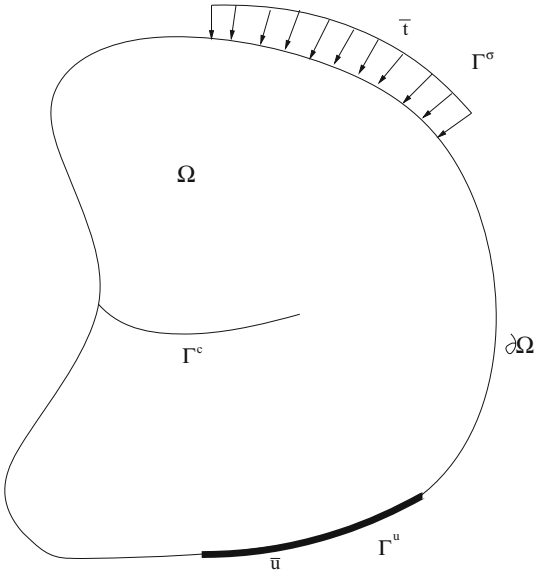

Fig. 1 Typical 3*D* LEFM boundary value problem

small deformations, the small-strain tensor is given by the symmetric component of the deformation gradient as

$$\boldsymbol{\varepsilon}(\boldsymbol{x}) = \frac{1}{2}\left[\nabla \boldsymbol{u} + \nabla \boldsymbol{u}^T\right]. \tag{3}$$

The following boundary conditions are enforced on the appropriate portions of $\partial\Omega$:

$$\boldsymbol{\sigma}(\boldsymbol{x})\boldsymbol{n}(\boldsymbol{x}) = \bar{\boldsymbol{t}}(\boldsymbol{x}, t) \quad \text{on} \quad \Gamma^{\sigma} \tag{4}$$

$$\boldsymbol{u}(\boldsymbol{x}) = \bar{\boldsymbol{u}}(\boldsymbol{x}) \quad \text{on} \quad \Gamma^{u} \tag{5}$$

$$\boldsymbol{\sigma}(\boldsymbol{x})\boldsymbol{n}(\boldsymbol{x}) = 0 \quad \text{on} \quad \Gamma^{c} \tag{6}$$

where $\bar{\boldsymbol{t}}(\boldsymbol{x}, t)$ are prescribed tractions and $\bar{\boldsymbol{u}}(\boldsymbol{x})$ are prescribed displacements. The boundary condition prescribed by (6) indicates a traction-free crack surface.

For a finite element formulation we seek the weak form of (1), which can be posed as:

$$\text{Find } \boldsymbol{u} \in \tilde{H}^1(\Omega) \text{ such that}$$
$$B(\boldsymbol{u}, \boldsymbol{v}) = L(\boldsymbol{v}) \;\forall\, \boldsymbol{v} \in H_0^1 \tag{7}$$

where $B(\cdot,\cdot)$ and $L(\cdot)$ are the bilinear and linear forms, respectively, and are given by

$$B(\boldsymbol{u}, \boldsymbol{v}) = \int_{\Omega} \boldsymbol{\sigma}(\boldsymbol{u}) : \boldsymbol{\varepsilon}(\boldsymbol{v})\, d\Omega$$
$$L(\boldsymbol{v}) = \int_{\Omega} \boldsymbol{f} \cdot \boldsymbol{v}\, d\Omega + \int_{\Gamma^{\sigma}} \bar{\boldsymbol{t}} \cdot \boldsymbol{v}\, d\Gamma. \tag{8}$$

We define the set of kinematically admissible displacement fields as

$$\tilde{H}^1(\Omega) = \left\{ \boldsymbol{u} \mid \boldsymbol{u}(\boldsymbol{x}) \in H^1(\Omega)\,;\, \boldsymbol{u}(\boldsymbol{x}) = \bar{\boldsymbol{u}}(\boldsymbol{x}) \quad \text{on } \Gamma^{u} \right\}$$

where H^1 is the first order Hilbert space. The space of kinematically admissible virtual displacement fields, $H_0^1(\Omega)$, is then defined as the subset of functions in $H^1(\Omega)$ which satisfy the homogeneous Dirichlet boundary conditions on Γ^u, i.e.

$$H_0^1(\Omega) = \left\{ \boldsymbol{v} \mid \boldsymbol{v}(\boldsymbol{x}) \in H^1(\Omega);\, \boldsymbol{v}(\boldsymbol{x}) = 0 \quad \text{on } \Gamma^{u} \right\}.$$

The above represents the weak formulation of a 3*D* elasticity problem for a standard finite element implementation. Generalized finite element shape functions (c.f. Sect. 3) are used to spatially discretize (7) in the usual manner.

2.2 Crack propagation considerations

There are many empirical fatigue crack growth laws available which are focused on the stable growth of macro-cracks subjected to cyclic loads of constant amplitude. In these instances, it may be appropriate to use the Paris–Erdogan equation (or something similar) for prediction of the crack growth rate [1,48] as a function of the variation in the locally extracted stress intensity factors (SIFs)

$$\frac{da}{dN} = C\,(\Delta K)^m \tag{9}$$

where $\frac{da}{dN}$ is the fatigue crack growth rate per loading cycle, $\Delta K = K_{max} - K_{min}$, is the stress intensity factor range during one cycle, and C and m are material parameters. The local SIF values may be computed from the finite element (FE) solution in the region of a crack front using either the contour integral or cut-off function methods as presented in the literature [24,50,63]. It may be noted that numerous other techniques are possible, but they are not used in this work.

An incremental algorithm for fatigue crack growth in linear elastic materials is adopted in this work. As such, the maximum crack front increment Δa_{max} is set at the beginning of each crack step. Fatigue life can then be estimated using an incremental form of (9),

$$N_i = N_{i-1} + \frac{\Delta a_{max}}{C\left(\Delta K_{eq}^{max}\right)^m} \tag{10}$$

where N_i and N_{i-1} are the number of cycles up to the current and previous crack advancement steps, respectively and K_{eq} is an equivalent effective SIF, defined subsequently, which takes into account K_I, K_{II} and K_{III}.

In a general $3D$ mixed-mode crack simulation, ΔK_{eq} can vary (perhaps quite significantly) along a particular crack front and therefore each crack front vertex will not propagate the same distance in a given crack advance step. The advancement of each vertex must be appropriately scaled so as to subject each crack front vertex to the same number of loading cycles, and thus allow for (9) to remain valid. In effect, the maximum crack increment size, Δa_{max}, is applied only to the crack front vertex that has maximum ΔK_{eq}, i.e., for which $\Delta K_{eq} = \Delta K_{eq}^{max}$. The crack growth increments for the other vertices are then scaled to match the number of cycles for the current step. Thus, for a given crack front vertex j, we can compute the advancement for the vertex as

$$\Delta a^j = C\left(\Delta K_{eq}^j\right)^m \frac{\Delta a_{max}}{C\left(\Delta K_{eq}^{max}\right)^m} = \Delta a_{max}\left(\frac{\Delta K_{eq}^j}{\Delta K_{eq}^{max}}\right)^m \tag{11}$$

where ΔK_{eq}^j is the variation of the equivalent stress intensity factor for vertex j.

The second major consideration for crack propagation simulations is the computation of the crack vertex deflection angles, and thus the crack propagation trajectory. In a purely continuum-level approach, as is the focus of the present work, crack growth direction may be computed from the extracted SIFs. In the general case, crack growth trajectory is defined by a kinking angle (θ) and twisting angle (ψ) at the crack front. In this paper, Schöllmann's criterion [57] is used for computation of the crack deflection angles.

Schöllmann's criterion [57] for crack path trajectory is based on the standard assumption that crack growth develops perpendicularly to the direction of a maximum applied principal stress σ_1'. The maximum principal stress, σ_1', is computed from the near field stresses σ_θ, σ_z and $\tau_{\theta z}$ as follows:

$$\sigma_1' = \frac{\sigma_\theta + \sigma_z}{2} + \frac{1}{2}\sqrt{(\sigma_\theta - \sigma_z)^2 + 4\tau_{\theta z}^2} \tag{12}$$

where σ_θ, σ_z and $\tau_{\theta z}$ are the components of the stress tensor, including the contributions of all three fracture modes. These stress components are defined in terms of the SIFs, and are computed in cylindrical coordinates as

$$\begin{aligned}
\sigma_\theta &= \frac{K_I}{4\sqrt{2\pi r}}\left[3\cos\left(\frac{\theta}{2}\right) + \cos\left(\frac{3\theta}{2}\right)\right] \\
&\quad - \frac{K_{II}}{4\sqrt{2\pi r}}\left[3\sin\left(\frac{\theta}{2}\right) + 3\sin\left(\frac{3\theta}{2}\right)\right] \\
\tau_{\theta z} &= \frac{K_{III}}{\sqrt{2\pi r}}\cos\left(\frac{\theta}{2}\right) \\
\sigma_z &= \frac{8\nu}{4\sqrt{2\pi r}}\left[K_I\cos\left(\frac{\theta}{2}\right) - K_{II}\sin\left(\frac{\theta}{2}\right)\right]
\end{aligned} \tag{13}$$

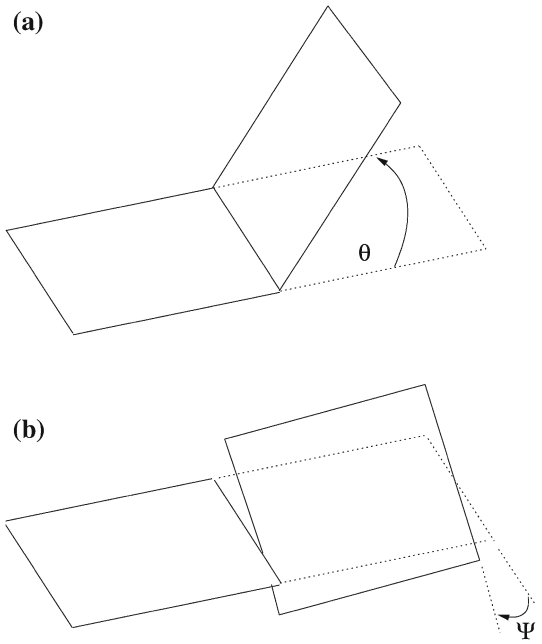

Fig. 2 Crack deflection angles computed to predict propagation path

Using Eqs. (12) and (13), the equivalent SIF, K_{eq}, can be computed for each crack front vertex as follows:

$$\begin{aligned}
K_{eq} = \frac{1}{2}\cos\left(\frac{\theta}{2}\right)\Bigg[K_I\cos^2\left(\frac{\theta}{2}\right) - \frac{3}{2}K_{II}\sin\left(\frac{\theta}{2}\right) \\
+ \sqrt{\left\{K_I\cos^2\left(\frac{\theta}{2}\right) - \frac{3}{2}K_{II}\sin\left(\frac{\theta}{2}\right)\right\}^2 + 4K_{III}^2}\Bigg]
\end{aligned} \tag{14}$$

K_{eq}^{max} is then used in (9) to compute the number of loading cycles corresponding to a given crack advancement. According to Schöllmann's criterion the crack growth deflection angles are calculated as follows. The kinking angle, θ, (Fig. 2a) is computed so as to satisfy

$$\frac{\partial \sigma_1'}{\partial \theta} = 0 \quad \text{and} \quad \frac{\partial^2 \sigma_1'}{\partial \theta^2} < 0 \tag{15}$$

The twisting angle, ψ, is then computed as

$$\psi = \frac{1}{2}\arctan\left[\frac{2\tau_{\theta z}(\theta)}{\sigma_\theta(\theta) - \sigma_z(\theta)}\right]. \tag{16}$$

Remark The crack propagation discussion has been included for completeness, but left intentionally brief. Detailed formulations of the crack propagation algorithm used in this paper along with the crack propagation criterion selected can be found in [52,57], respectively. A detailed account of SIF extraction appropriate for GFEM can be found in [50].

3 Generalized finite element method: an overview

The generalized finite element method (GFEM) [17] is a partition-of-unity (PoU) based FE method [19,42]. The GFEM is similar in nature to the standard, Galerkin FE method [6], but offers significant flexibility in terms of shape function construction. For a given node α in a FE mesh, we can define a GFEM shape function as

$$\phi_{\alpha i}(\boldsymbol{x}) = \varphi_\alpha(\boldsymbol{x}) L_{\alpha i}(\boldsymbol{x}) \tag{17}$$

where there is no implied summation on α.

The GFEM shape functions have two distinct components, each providing a benefit. The first component, $\varphi_\alpha(\boldsymbol{x})$, is referred to as a PoU function. This simply implies that the function sums to one at any point in the domain, i.e.

$$\sum_{\alpha=1}^{N} \varphi_\alpha(\boldsymbol{x}) = 1, \quad \forall\, \boldsymbol{x} \in \Omega. \tag{18}$$

Within the *GFEM* context, the PoU functions are provided by standard, Langrangian FE shape functions.

The second component of the GFEM shape functions are called *enrichment functions*, $L_{\alpha i}(\boldsymbol{x})$. The enrichment functions are local approximation spaces which are a priori known to approximate well the physics of the given problem locally. Both components of the GFEM shape function contribute a specific benefit which is leveraged in the resulting GFEM approximation. The compact support of the PoU functions provide the benefit that the global approximation space inherits the inter-element continuity of the PoU functions, even though in general, the enrichment functions will not satisfy global conformity on their own [42]. The global approximation space also inherits the local approximation potential of the enrichment functions because the PoU used to paste them together can exactly reproduce the shape of the enrichment functions in the global approximation space. It is this second attribute of the global GFEM approximation space which is the focal point of this work as well as most of the previous work in the GFEM.

The GFEM has been applied successfully to numerous engineering applications. These application areas include, but are not limited to: the simulation of boundary layers [15], dynamically propagating fractures [18], singularities in structural mechanics problems [17], high wave number acoustics [4,41], advection-diffusion equations with high Peclet number [65], materials with polycrystalline microstructures [58], porous materials [60], $3D$ LEFM [51], $3D$ crack propagation in a linear elastic medium [52].

A benefit of the GFEM is that it sits atop a robust mathematical foundation [3,17,42,43,61], which is in contrast to many other multi-scale FE approaches. As a result, an error bound has been derived for the global approximation error within the GFEM. The error bound may be formally posed as

Theorem *Let $u \in H^1(\Omega)$. Then there is $u_{hp} \in S^{GFEM}$ such that*

$$\|u - u_{hp}\|^2_{H^1(\Omega)} \leq \hat{C} \sum_{\alpha=1}^{N} \inf_{u_\alpha \in \chi_\alpha} \|u - u_\alpha\|^2_{H^1(\omega_\alpha)}.$$

Proof of the theorem can be found in the literature [42]. In the above theorem, S^{GFEM} is the GFEM solution space, $\hat{C}$ is a problem-dependent constant, and $\|\cdot\|$ denotes an energy norm.

What the error bound essentially indicates is that the resulting global error is bounded by the local errors, and thus the GFEM relies upon the availability of a high-quality enrichment basis in order to guarantee accurate solutions. Unfortunately, in many cases, high quality, closed-form, analytical enrichment functions are not available a priori. This is true, for instance, in the case in which there are multiple crack surfaces within close proximity to one another, which is one application area considered in this paper. Other scenarios lacking closed form analytical enrichments include, but are not limited to: problems involving nonlinearities, dynamics or general multi-scale applications; all of which are important to the engineering design and analysis communities. As such, we would like to extend the range of applicability of the GFEM to be more appropriate for these types of applications.

Due to the GFEM 's reliance upon high quality enrichment functions in order to ensure good global accuracy, and the limited availability of closed-form analytical enrichment functions, a more general version of enrichment function construction is required. A more general extension of the GFEM, referred to as the generalized finite element method with global-local enrichment functions (GFEM$^{\text{gl}}$) [16,33] has been proposed. In the GFEM$^{\text{gl}}$ framework, enrichment functions are numerically generated on-the-fly during the course of the simulation, and customized to resolve the localized physics of the particular problem being analyzed. The GFEM$^{\text{gl}}$ can be seen as simply a more general form of the standard GFEM. A brief overview of the GFEM$^{\text{gl}}$ is now presented.

4 Generalized finite element method with global-local enrichments

The GFEM$^{\text{gl}}$ [16,33] is a more general version of the standard GFEM aimed at alleviating the a priori requirement of a high quality local approximation space. The essential idea of the method is to build specially-tailored enrichment func-

tions to allow for accurate analyses on fixed, coarse meshes. In the GFEM^{gl}, two discretizations are utilized: (1) fixed, coarse global discretization and (2) highly-adapted, potentially evolving local discretization defined in a region of localized interest. Each discretization constitutes a separate, but linked BVP to be analyzed. The following is a formulation of the GFEM^{gl} with global hexahedral elements appropriate for LEFM applications. A detailed formulation for transient heat conduction can be found in [46]. While beyond the scope of the current paper, the GFEM^{gl} approach has also been successfully developed for nonlinear applications involving small-strain plasticity models [28,35] as well as propagating cohesive fractures [36], with the use of *tetrahedral* elements in both the global and local domains.

Initial global problem The initial phase of the GFEM^{gl} involves the solution of the 3D elasticity problem posed in Sect. 2 on a coarse FE mesh, in this case composed of hexahedral elements. The crack itself is not modeled directly in the global BVP, taking the same approach as was used in [33], which indicates that $\Gamma^c = \emptyset$ in Fig. 1.

The initial global BVP to be solved in order to generate boundary conditions with which to drive the computation of the global-local enrichment functions is formally posed as:

$$\begin{aligned}&\text{Find } \boldsymbol{u}^G \in \chi^G(\Omega) \subset \tilde{H}^1(\Omega) \text{ such that } \forall \boldsymbol{v}^G \in \chi^G(\Omega)\\ &\int_\Omega \boldsymbol{\sigma}\left(\boldsymbol{u}^G\right) : \boldsymbol{\varepsilon}\left(\boldsymbol{v}^G\right) d\Omega + \eta_p \int_{\Gamma^u} \boldsymbol{u}^G \cdot \boldsymbol{v}^G d\Gamma\\ &= \int_\Omega \boldsymbol{f} \cdot \boldsymbol{v}^G \, d\Omega + \int_{\Gamma^\sigma} \bar{\boldsymbol{t}} \cdot \boldsymbol{v}^G \, d\Gamma + \eta_p \int_{\Gamma^u} \bar{\boldsymbol{u}} \cdot \boldsymbol{v}^G d\Gamma.\end{aligned} \tag{19}$$

We can more stringently define the FE solution space as

$$\chi^G(\Omega) = \left\{ \boldsymbol{u}^G = \sum_{\alpha=1}^{N^G} \varphi_\alpha(\boldsymbol{x}) \hat{\boldsymbol{u}}_\alpha \right\} \tag{20}$$

in which N^G is the number of nodes in the global mesh and the PoU functions, $\varphi_\alpha(\boldsymbol{x})$ are provided by either tri-linear (c.f.(21)) or tri-quadratic hexahedral elements. The use of the η_p parameter in (19) is indicative of a penalty formulation used to enforce Dirichlet boundary conditions. Other methods may be used for the application of this boundary condition type, but in this instance the penalty method is used due to ease of implementation. For clarity of presentation, the global PoU functions shown in (20) corresponding to the use of 8-node brick elements are the standard Lagrangian shape functions as can be found in most finite element text books, for instance [13]. The shape functions are explicitly defined as

$$\{\boldsymbol{N}\} = \left\{ \begin{array}{l} \frac{1}{8}(1-\xi)(1-\eta)(1-\zeta) \\ \frac{1}{8}(1+\xi)(1-\eta)(1-\zeta) \\ \frac{1}{8}(1+\xi)(1+\eta)(1-\zeta) \\ \frac{1}{8}(1-\xi)(1+\eta)(1-\zeta) \\ \frac{1}{8}(1-\xi)(1-\eta)(1+\zeta) \\ \frac{1}{8}(1+\xi)(1-\eta)(1+\zeta) \\ \frac{1}{8}(1+\xi)(1+\eta)(1+\zeta) \\ \frac{1}{8}(1-\xi)(1+\eta)(1+\zeta) \end{array} \right\}. \tag{21}$$

Local problem Once the initial global BVP is solved, the local BVP can then be solved in order to compute the global-local enrichment functions. The local domain itself, Ω^L, is created as a subset of global elements consisting of the global elements containing the crack surface itself. After the elements comprising the local domain have been selected, the coarse global elements are converted from hexahedral elements to tetrahedral elements using the *smallest vertex* algorithm [14]. With this particular conversion technique, no neighbor information is required to ensure a conforming tetrahedral mesh when converting a hexahedral element. This aspect of the algorithm makes it very appealing for the element conversion process, which is illustrated in Fig. 3b, c.

A subtle yet important detail of the methodology is the automatic subdivision of the global hexahedral elements into nested, local tetrahedral elements. The nesting of local elements facilitates the accurate integration of the enriched global weak form. Similar to that which is presented in great detail in [33], the enriched global shape functions are integrated using the integration points from the local elements. In this instance, further clarification may be beneficial, since multiple levels of local integration rules are required, as shown in Fig. 4. In the far left of the figure, the global hexahedral element has been subdivided into tetrahedral elements, and uniformly refined. Additional refinement is then performed on the light green region, to generate a locally graded mesh in the region of the crack front. Refined elements in the light green region indicate more integration points per element, indicative of potentially using higher order enrichment functions in this region. No further computational elements are generated at this point, but additional *integration elements* are created for elements which are cut by the crack surface, or contain the crack front, as presented in great detail in [51]. It is the generation of the *integration elements* which allows for the accurate integration of the discontinuous and singular enrichment functions used to model the crack surface within the elements themselves (discussed more below). Integration rules for the local elements which directly interact with the crack surface/front are only provided by the *integration elements*, as these are used in replace of, not in addition to, the integration rules which would be provided by the locally

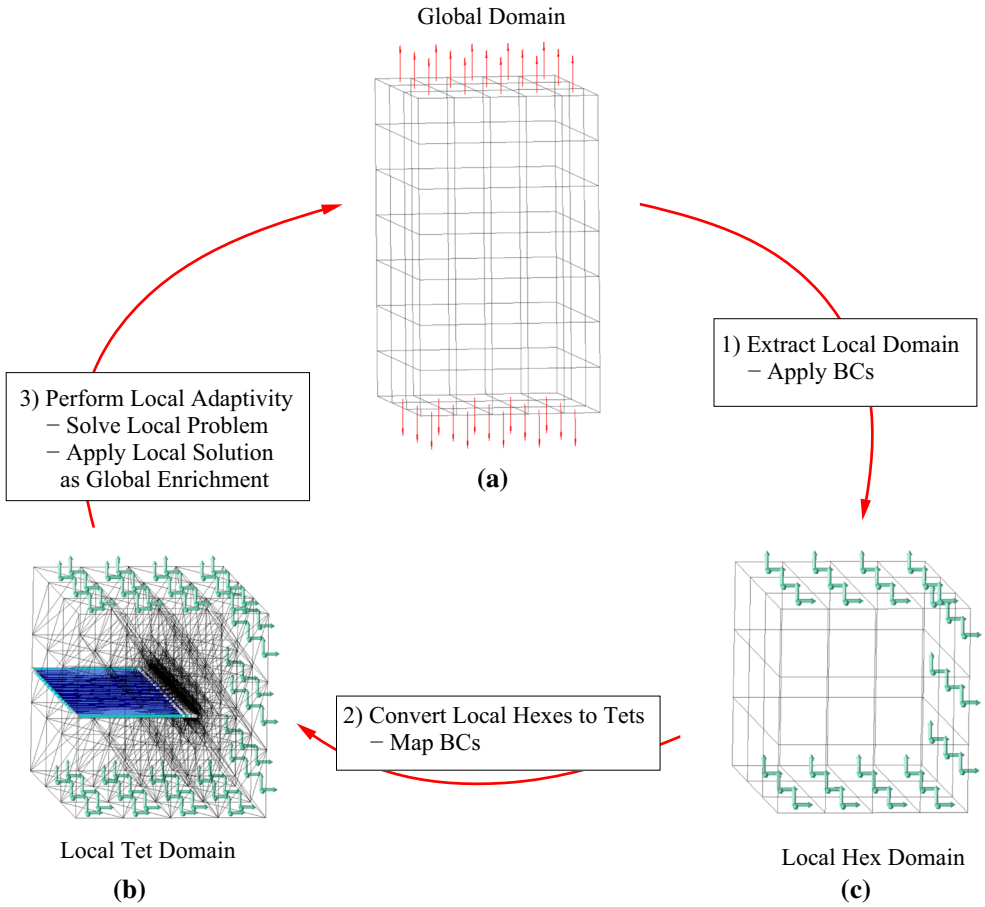

Fig. 3 Illustration of the $GFEM^{gl}$ with global hexahedral elements used for LEFM analyses in this paper

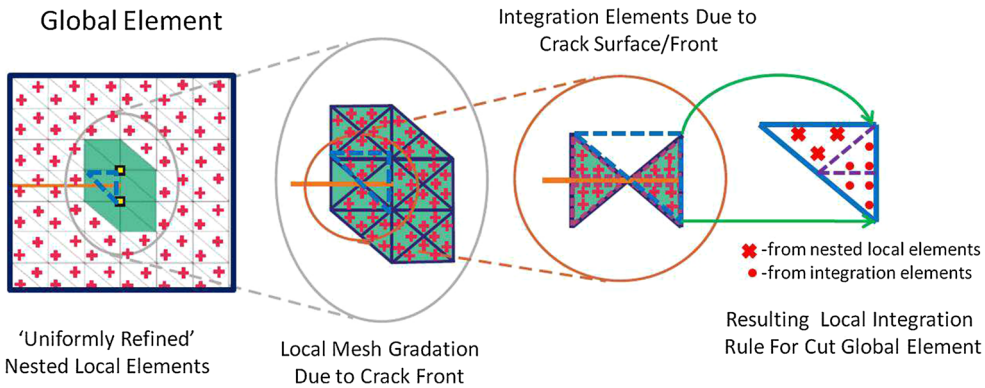

Fig. 4 Illustrates the different levels of local elements used to accurately integrate out the local enrichment functions for use in the enriched global problem

refined, but uncut (i.e. before being diced into *integration elements*), nested local elements. Special quadrature rules designed for efficient numerical integration of singular functions, such as those presented in [49], are also available for use. One representative local tetrahedral region's integration rule is shown at the far right in the figure, in which integration points are generated due to both the local gradation of the mesh, as well as the cutting of a tetrahedral element into *integration elements*. One additional note, as is discussed in [51], *integration elements* in the vicinity of the crack front will utilize a higher order integration rule to accurately integrate the singular terms present in the tip enrichment functions.

The numerical integration of the enriched global hexahedral elements is then done using all of the locally generated integration points (all red glyhps in the figure). The nesting of the locally generated integration elements signifi-

cantly facilitates selection of the enriched global integration rules which are subsequently used in the enriched global problem.

If the local elements are not nested in the global discretization, the integration of the enriched elements, and thus the up-scaling of information through the use of the local solution, $\boldsymbol{u}^L$, as enrichment (c.f. Sect. 4) becomes very difficult. It is possible that significant amounts of information may be lost due to integration errors, and the accurate multi-scale aspect of the approach would be compromised.

An important feature of the local BVP, as defined in (22), is the use of the global displacement field, $\boldsymbol{u}^G$, as boundary conditions applied at the local boundary which are interior to the global domain, so as to drive the local BVP. In this manner, information is transferred from the global BVP level down to the local BVP level. Different types of global-local boundary conditions are possible for use at the local domain boundary [33], but only Dirichlet are used in the present work. Portions of the local boundary which intersect the global boundary are subjected to boundary conditions which come directly from the global BVP.

The local boundary value problem to be solved in order to generate the global-local enrichment function is formally posed as:

$$\begin{aligned}
&\text{Find } \boldsymbol{u}^L \in \chi^L(\Omega^L) \subset \tilde{H}^1\left(\Omega^L\right)\\
&\quad \text{such that } \forall \boldsymbol{v}^L \in \chi^L(\Omega^L)\\
&\int_{\Omega^L} \boldsymbol{\sigma}\left(\boldsymbol{u}^L\right) : \boldsymbol{\varepsilon}\left(\boldsymbol{v}^L\right) d\Omega + \eta_p \int_{\Gamma^L \setminus (\Gamma^L \bigcap \Gamma^\sigma)} \boldsymbol{u}^L \cdot \boldsymbol{v}^L d\Gamma\\
&= \int_{\Omega^L} \boldsymbol{f} \cdot \boldsymbol{v}^L \, d\Omega + \int_{\Gamma^L \bigcap \Gamma^\sigma} \bar{\boldsymbol{t}} \cdot \boldsymbol{v}^L \, d\Gamma\\
&\quad + \eta_p \int_{\Gamma^L \bigcap \Gamma^u} \bar{\boldsymbol{u}} \cdot \boldsymbol{v}^L d\Gamma + \eta_p \int_{\Gamma^L \setminus (\Gamma^L \bigcap \partial\Omega)} \boldsymbol{u}^G \cdot \boldsymbol{v}^L d\Gamma.
\end{aligned} \tag{22}$$

In this instance we define the local GFEM solution space as

$$\chi^L(\Omega^L) = \left\{ \boldsymbol{u}^L = \sum_{\alpha=1}^{N^L} \varphi_\alpha^L(\boldsymbol{x}) \left[\boldsymbol{u}_\alpha^p(\boldsymbol{x}) + \mathscr{H}\hat{\boldsymbol{u}}_\alpha(\boldsymbol{x}) + \tilde{\boldsymbol{u}}_\alpha(\boldsymbol{x}) \right] \right\} \tag{23}$$

in which the PoU functions defined on Ω^L, $\varphi_\alpha^L(\boldsymbol{x})$, are provided by linear 4-node tetrahedral elements as presented in many finite element text books, such as [13]. The local PoU functions are defined explicitly with respect to the parent element coordinate system as

$$\{\boldsymbol{N}\} = \begin{Bmatrix} 1-\xi-\eta-\zeta \\ \xi \\ \eta \\ \zeta \end{Bmatrix}. \tag{24}$$

The conversion from hexahedral elements to tetrahedral elements in the local BVP is what allows for the crack surface to be modeled using the *hp-GFEM* as presented in [51], which is implied in (23). The discontinuity surface itself is modeled through the use of discontinuous Heaviside enrichments applied to nodes whose support is fully cut by the crack surface ($\mathscr{H}\hat{\boldsymbol{u}}_\alpha(\boldsymbol{x})$). Nodes whose supports contain the crack front are enriched with the asymptotic expansions for a sharp crack in a $2D$ elastic medium ($\tilde{\boldsymbol{u}}_\alpha(\boldsymbol{x})$), as can be found in [51]. The $\boldsymbol{u}_\alpha^p(\boldsymbol{x})$ term in (23) is representative of the potential use of higher order, continuous polynomial enrichment functions to raise the order of the resulting *GFEM* approximation space used in the local BVP, again as presented in [51].

With this enrichment strategy, the crack surface may be modeled completely independent of the underlying FE mesh. The mesh itself is locally graded in the region of the crack front to better resolve the sharp gradients arising in the region near the crack tip. A locally graded mesh in the near crack tip region is still required along with the proper enrichment strategy in order to obtain high levels of accuracy. The reason for the necessity of local mesh refinement lies in the fact that the enrichment functions come from the $2D$ elasticity solution and not a $3D$ solution. Even so, the use of this asymptotic expansion as enrichment has seen widespread use within the GFEM and XFEM communities [7,51] in both 2D and 3D applications. 3D asymptotic expansions, while they could be possible, are quite complex, especially in regions where the crack surface intersects the domain boundary and the type of singularity itself changes. In fact, $3D$ problems would require the use of additional, complementary expansions, termed 'Shadow Functions' [10,67] to retain strict validity as high quality enrichment functions for $3D$ applications. Therefore, it is more practical to use $2D$ expansions of the elastic solution as enrichment functions. As a result, in order to obtain acceptable accuracy in fully $3D$ analyses it is necessary to have a sufficiently refined mesh around the crack front to properly resolve the highly localized gradients which develop in the region.

It is the requirement of a highly adapted local model which naturally leads to the use of tetrahedral elements in the local BVP mesh. Tetrahedral elements allow for a straightforward refinement scheme based on the marked edge algorithm [2,5] which generates highly graded, conforming meshes whose element quality is no worse than the element quality of the initial, coarse discretization. As noted previously, this type of locally-graded mesh (without irregularity) is in general not possible with the use of hexahedral elements [11,12].

While a highly adapted, and therefore potentially computationally expensive, local BVP seemingly poses a limitation to the efficiency of the approach, a parallel decomposition of the local domain for computation of the enrichment functions has been proposed. The approach has been proposed and investigated for both LEFM applications [34] as well as multi-physics applications [54] and in both instances preliminary results indicate that good parallel efficiency is attainable. A more thorough investigation of the parallel approach is the focus of future investigations.

Another benefit of the conversion of hexahedral to tetrahedral elements in the local domain, as previously alluded to, in addition to the potential for a highly adapted mesh, is the potential to use the meticulously developed crack surface geometry engine presented in [51] for tetrahedral elements. The computational geometry engine allows for the automatic selection of the proper enrichment functions to explicitly represent the crack surface; the dicing of cut elements into integration elements; automated selection of localized regions of high refinement around crack fronts; and the ability to accurately extract mixed-mode SIF values at any crack front vertex and advance the crack front vertices based on the appropriate physics. With the proposed use of the tetrahedral elements in the local domain, all of these features are readily available to compute enrichment functions to allow for accurate crack surface representation and LEFM analyses on fixed, coarse hexahedral meshes.

Enriched global problem Once the local BVP has been solved, we once again re-solve the global BVP using the local solution, $\boldsymbol{u}^L$ as our multi-scale enrichment function. We refer to this as the enriched global problem. We formally pose the BVP as:

$$\begin{aligned}&\text{Find } \boldsymbol{u}^E \in \chi^E(\Omega) \subset \tilde{H}^1(\Omega) \text{ such that } \forall \boldsymbol{v}^E \in \chi^E(\Omega)\\ &\int_\Omega \boldsymbol{\sigma}\left(\boldsymbol{u}^E\right) : \boldsymbol{\varepsilon}\left(\boldsymbol{v}^E\right) d\Omega + \eta_p \int_{\Gamma^u} \boldsymbol{u}^E \cdot \boldsymbol{v}^E d\Gamma\\ &= \int_\Omega \boldsymbol{f} \cdot \boldsymbol{v}^E \, d\Omega + \int_{\Gamma^\sigma} \bar{\boldsymbol{t}} \cdot \boldsymbol{v}^E \, d\Gamma + \eta_p \int_{\Gamma^u} \bar{\boldsymbol{u}} \cdot \boldsymbol{v}^E d\Gamma.\end{aligned} \tag{25}$$

We now define the enriched global GFEM solution space as

$$\chi^E(\Omega) = \left\{ \boldsymbol{u}^E = \sum_{\alpha=1}^{N^G} \varphi_\alpha(\boldsymbol{x}) \hat{\boldsymbol{u}}_\alpha + \sum_{\beta \in \mathscr{I}_E} \varphi_\beta(\boldsymbol{x}) \boldsymbol{u}_\beta^{gl}(\boldsymbol{x}) \right\} \tag{26}$$

in which $\mathscr{I}_E$ is the set of global nodes enriched with $\boldsymbol{u}^L(\boldsymbol{x})$, $\varphi_\alpha(\boldsymbol{x})$ and $\varphi_\beta(\boldsymbol{x})$ are global PoU functions provided by hexahedral elements (c.f.(21)) and the term $\boldsymbol{u}_\beta^{gl}(\boldsymbol{x}) = \{u_\beta u_L^u(\boldsymbol{x}), v_\beta u_L^v(\boldsymbol{x}), w_\beta u_L^{w(\boldsymbol{x})}\}^T$. The terms $u_L^u(\boldsymbol{x})$, $u_L^v(\boldsymbol{x})$, $u_L^w(\boldsymbol{x})$ are the components of the local solution vector, $\boldsymbol{u}^L(\boldsymbol{x})$, taken with respect to the global coordinate system, and u_β, v_β, w_β are global Dofs. The local solution vector, $\boldsymbol{u}^L(\boldsymbol{x})$, is defined as in (23) and has the local PoU functions (c.f.(24)), $\varphi^L(\boldsymbol{x})$, provided by tetrahedral elements embedded within, so the resulting solution space is built with two different types of PoU functions. Through the use of the multi-scale global-local enrichment functions, $\boldsymbol{u}^L(\boldsymbol{x})$, the enriched global BVP now has the crack surface modeled entirely through enrichment, with $\boldsymbol{u}^L(\boldsymbol{x})$ computed using the *hp-GFEM* as formulated for tetrahedral elements. In accordance with previous works [16,33], the local solution is a numerically computed function which may be evaluated at any location in Ω_L. The function itself may thus be evaluated at any integration point when its contributions to the global weak form are numerically integrated out in (25). The numerically generated enrichment function is simply a FE solution, computed with known approximating functions, (23). As such the derivatives of the local solution can also be computed, or more specifically evaluated at integration points, for use in the gradient terms arising in (25).

It should be noted that similar to the approach taken in [46], in the creation of the local problem, only the corner nodes of the global hexahedral elements are used for the conversion into tetrahedral elements. It is important to note that all global nodes encompassed by the local domain are enriched with the local solution. That is to say that even though mid-edge and face nodes from a higher order hexahedral element are not used in the creation of the local tetrahedral domain, they *are still enriched* with the local solution so as to preserve the PoU property of the shape functions used to accurately paste the local solution into the enriched global approximation space.

To summarize the overall algorithm, Fig. 3 illustrates the basic flow of the GFEM^{gl} methodology: (1) extract local BVP as a subset of elements from the global model and apply boundary conditions derived from global BVP solution; (2) convert hexahedral elements to tetrahedral elements to allow for a locally graded mesh; (3) solve local BVP and apply local solution as enrichment for the global solution space.

We now analyze several numerical examples to evaluate the accuracy of the proposed GFEM^{gl} methodology with global hexahedral elements. Numerical examples are analyzed which illustrate the truly multi-scale potential of the GFEM^{gl} enrichment functions when very coarse global elements are utilized. The term 'very coarse' will be seen to indicate scenarios in which pertinent crack surface geometry features (such as kinks), or multiple crack surfaces, are accurately represented within one computational element.

5 Numerical experiments

In this section we analyze a series of LEFM problems demonstrating the capability of the method to handle benchmark

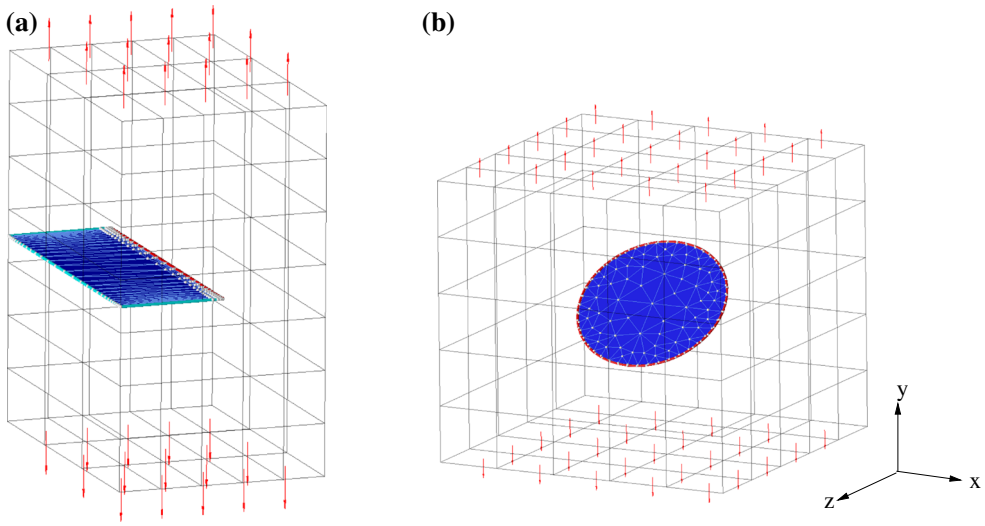

Fig. 5 Model problems used to assess the use of a coarse, uniform hexahedral mesh for GFEM^{gl} fracture analyses. The problems selected illustrate simple Mode I (**a**) and fully mixed-mode (**b**) scenarios. **a** Through-thickness edge crack. **b** Inclined penny-shaped crack

Table 1 Problem details for Benchmark 1 and Benchmark 2

	E	ν	Dimensions (x, y, z)	Crack length (a)
Benchmark 1	2e5 psi	0.333	(2.0 in, 3.5 in, 3.0 in)	1.0 in
Benchmark 2	1e3 psi	0.300	(4.0 in, 4.0 in, 4.0 in)	1.0 in

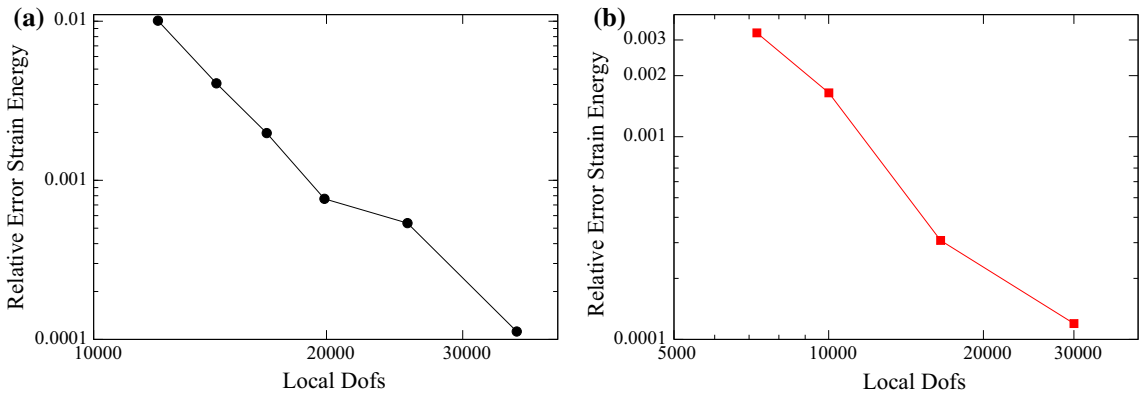

Fig. 6 Convergence in the enriched global strain energy corresponding to an h-extension in the local domain. Error values are computed with reference to an overly refined hp-GFEM solution. **a** Benchmark 1. **b** Benchmark 2

caliber static fracture, multi-site damage and mixed-mode crack propagation scenarios. An application problem involving the analysis of a representative aircraft-type structure is also provided. The examples are selected so as to demonstrate the ability of the *GFEM*^{gl} to accurately assess fully mixed-mode fracture scenarios as well as multiple-site damage analyses and crack propagation simulations utilizing a fixed, coarse hexahedral mesh. Unless otherwise noted, only one global-local iteration is used in the following numerical experiments. Detailed analysis of the impact that multiple global-local iterations can have on enriched global solution accuracy can be found in [29,45].

5.1 Static crack Benchmark problems

Figure 5 illustrates two benchmark problems involving static fracture analyses which are analyzed for numerical verification purposes. The model problem shown in Fig. 5a (Benchmark 1) is a simple Mode I problem, whereas the model problem illustrated in Fig. 5b (Benchmark 2) represents a fully mixed-mode scenario where all three fracture modes are both present and relevant. These benchmark example problems illustrate the ability of the method to accurately extract all three SIF values on a coarse hexahedral mesh. The extracted values can then be used in (9)

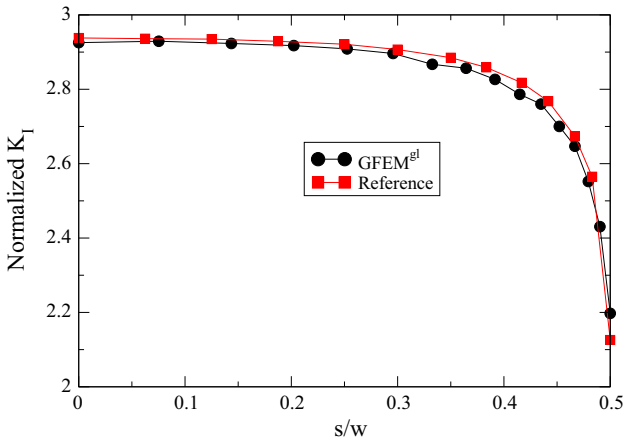

Fig. 7 Normalized K_I plotted along crack front. The point with $s = 0.0$ corresponds to the center of the crack front

and (13) to predict both loading cycles accumulated as well as crack trajectories in fatigue crack propagation analyses.

In both model problems the domain is subjected to unit, normal tractions applied to the top and bottom faces of the domain, shown as red arrows in Fig. 5. Point Dirichlet boundary conditions are applied so as only to prevent rigid body motions. The material properties, as well as geometric dimensions are provided for each model in Table 1. For *Benchmark* 2, the crack length corresponds to the crack radius, and the crack surface is inclined counter-clockwise at an angle, $\alpha = 45°$ with respect to the global z-axis. Both model problems utilize a uniform mesh comprised of 27-node hexahedral elements. As a note, all numerical examples presented in this section utilize the same global coordinate axes as are shown in Fig. 5b.

The examples presented in this section, as well as subsequent, utilize a local discretization which has been enriched to a resulting polynomial order of, $p = 3$. The *only* enrichments applied to the global, hexahedral models are the global-local enrichment functions, i.e. u^L, and no additional polynomial or non-polynomial enrichment functions are used in the global models. It may also be noted that the global, hexahedral models utilize 27-node hexahedral elements, with the exception of the stiffened panel (c.f. Sect. 5.4) which is composed of 20-node hexahedral elements.

Convergence in the enriched global strain energy value corresponding to an h-extension in the local domain is presented in Fig. 6a. A reference strain energy value for Benchmark 1 was computed using hp-GFEM as presented in [51] with an overly refined mesh utilizing 772,038 dofs. It can be seen from the plot that the strain energy converges monotonically with local mesh refinement, and it may be noted that the enriched global problem has 4620 dofs, regardless of the level or refinement used in the local problem.

The normalized Mode I SIF

$$\bar{K_I} = \frac{K_I}{\sigma_0 \sqrt{\pi a}} \tag{27}$$

in which σ_0 is the applied traction and a is the crack length, was computed at each crack front vertex. As a note, in the two benchmark problems in this section, the extraction of SIFs is performed using the cut-off function method [24,50,63] for all relevant fracture Modes.

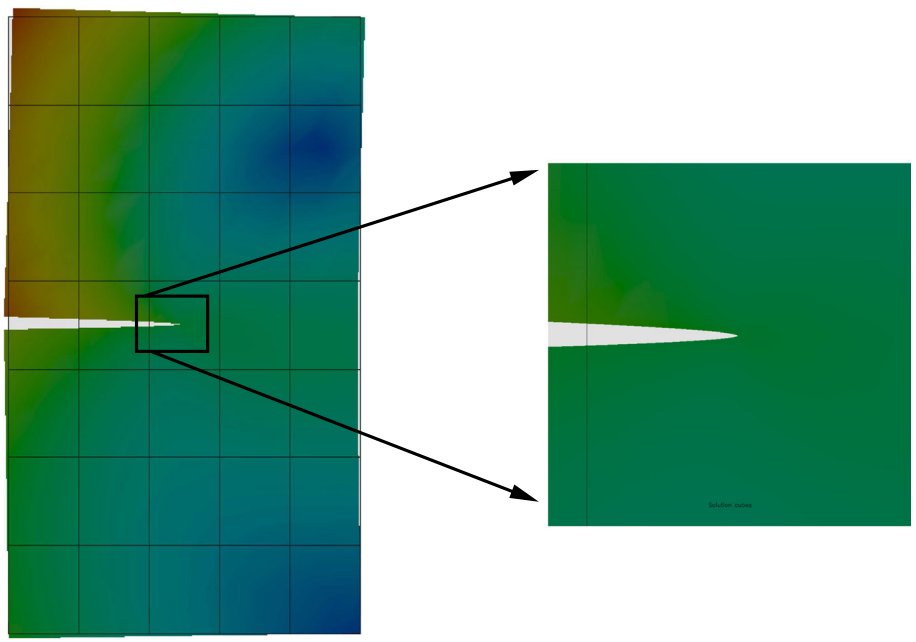

Fig. 8 Enriched global displacement contour computed on a hexahedral mesh. Note that the elements shown in the figure are the actual computational elements used to generate the displacement contour

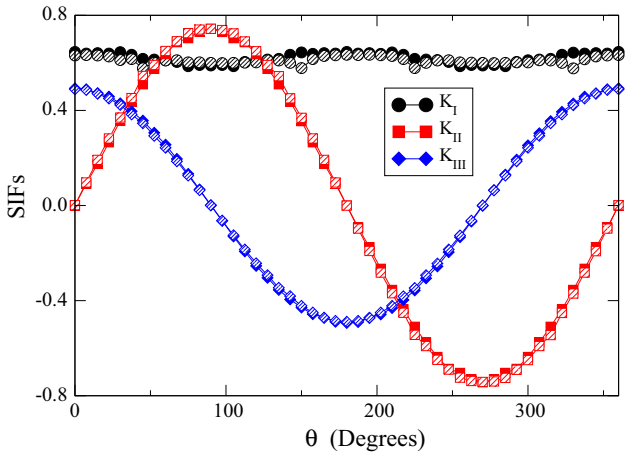

Fig. 9 Extracted SIF values along crack front. *Solid glyphs* denote data from reference solution and *hashed glyphs* represent data generated with $GFEM^{gl}$ analyses on a coarse hexahedral mesh

The normalized Mode I SIF values are plotted in Fig. 7 along the crack front. A reference curve is also provided in the figure, which was obtained from [39] where the authors analyzed the problem using the boundary element method. As can be seen, the normalized Mode I SIFs computed with the GFEM^{gl} compare very well with the reference curve, and capture the edge effects as the crack vertices approach the domain boundary. Figure 8 shows the enriched global displacement contour for Benchmark 1, and as can be seen the Mode I crack opening is accurately represented on the coarse, hexahedral mesh, without the requirement of any global mesh refinement or any requirement of the crack surface lining up with element faces in the global mesh.

Benchmark 2 presents a mixed-mode fracture problem, due to the inclination of the crack with respect to the loading axis. Convergence in the enriched global strain energy value again corresponding to an h-extension in the local domain is presented in Fig. 6b. The reference strain energy value for *Benchmark* 2 was also computed using hp-GFEM with a model consisting of 528,408 dofs. It can be seen that the strain energy again converges to the reference value with local mesh refinement. In this benchmark problem the enriched global problem has 6180 dofs.

Modes I, II and III SIFs are extracted along the crack front, and plotted in Fig. 9. A reference solution for each of the SIF curves is also plotted in the figure. The reference solution is computed using the hp-GFEM as in [52]. In that work the *hp-GFEM* solution was shown to be very accurate as compared to an analytical solution obtained from [64], and can thus be taken as a reliable reference. The solid glyphs on the plot represent the reference data, whereas the hashed glyphs denote data generated with $GFEM^{gl}$ and hexahedral elements. As can be seen, there is very good quantitative agreement between the two sets of data.

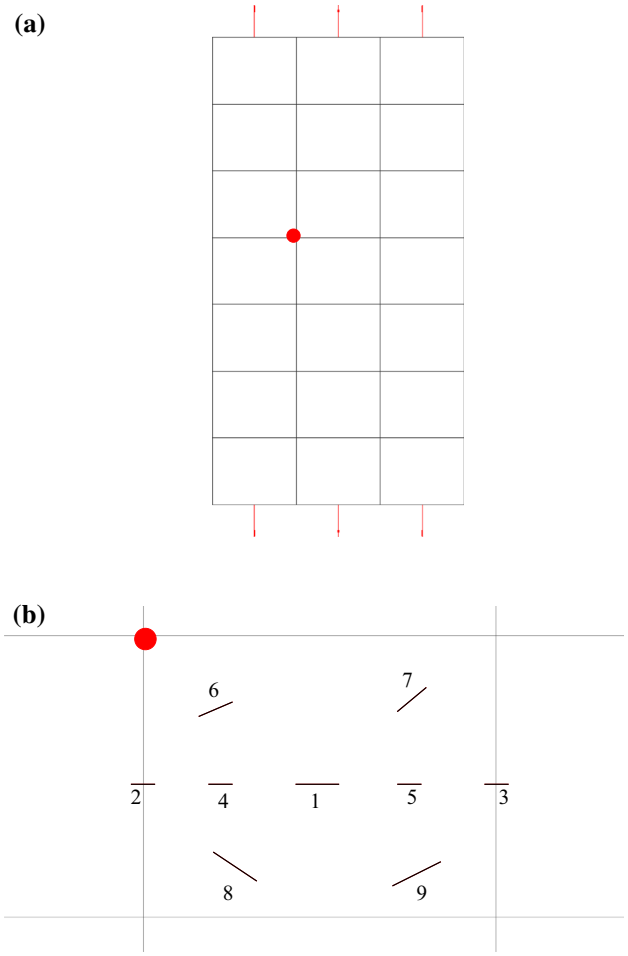

Fig. 10 $GFEM^{gl}$ model used for multi-site damage simulation. The *red glyphs* represent the common geometric point in both figures. **a** Model with boundary conditions. **b** Zoomed-in view of cracked configuration. (Color figure online)

5.2 Static, multi-site damage analysis

The example problem in this section investigates a multi-site damage scenario involving multiple, static crack surfaces. This example seeks to illustrate the ability of the GFEM^{gl} to analyze multiple discontinuity surfaces in close proximity to one another. The ability to analyze multiple discontinuity surfaces within one computational element allows for analyses on significantly coarser meshes, and thus more efficient analyses than would otherwise be possible with standard FE approaches. In his instance, the increased generality of the GFEM^{gl} over the standard GFEM is highlighted, as there are no general, closed-form analytical enrichment functions readily available for use in a problem with multiple cracks in close proximity. We are relying on the more flexible, numerically-generated multi-scale nature of the enrichment functions to deliver accurate results for this class of problems analyzed on coarse FE meshes. The proposed method may be seen as a potential alternative approach to address

Table 2 Details of crack Configuration for Multi-Site Damage Simulation

Crack	(x, y)	α	$2a$
1	(0,0)	0	0.15
2	$(-0.25, 0)$	0	0.05
3	(0.25,0)	0	0.05
4	$(-0.15, 0)$	0	0.05
5	(0.15,0)	0	0.075
6	$(-0.15, 0.14)$	20	0.159
7	(0.16,0.12)	45	0.127
8	$(-0.1, -0.15)$	-30	0.173
9	$(0.17, -0.09)$	25	0.166

Values are reported in inches and degrees

the class of multi-site damage simulations which are investigated with the multi-scale projection method by Loehnert and co-workers [30,31,40].

The domain has dimensions $(1.5 \times 2.8 \times 0.125)$ inches in the x-, y- and z-directions, respectively. The domain is subjected to normal tractions of magnitude $100\,psi$ along the top and bottom faces, as indicated by the red arrows in Fig. 10a. Young's Modulus is taken as $E = 17,100\,ksi$ and Poisson's ratio is taken as, $\nu = 0.325$.

Crack configuration details are provided in Table 2. The angle of inclination, α, is taken positive counter-clockwise with respect to the x-axis. The values reported for (x, y) indicate the coordinates of the center of the crack surface, with the origin taken as the center of $Crack\ 1$. The center of $Crack\ 1$ lines up with the center of the domain. The value reported as $2a$ indicates the total crack length.

The representation of multiple crack surfaces in close proximity to one another is a non-trivial task, particularly on a coarse FE mesh. As is noted in [25], the use of an explicit crack surface representation in conjunction with a locally graded mesh greatly facilitates this type of analysis. As such, in this instance we rely on the highly graded local mesh to generate the enrichment functions representing the multiple discontinuity surfaces in close proximity to one another. We then utilize the truly multi-scale nature of the GFEM^{gl} approach to accurately represent the multi-site damage scenario on an extremely coarse FE mesh. As can be seen in Fig. 11 we require *no local mesh refinement* in order to represent the multiple discontinuity surfaces, which are in this case all within *one computational element.*

A reference solution was generated for the same problem using *hp-GFEM*, and an overly refined model consisting of $1,722,426$ dofs. The enriched global problem utilizes $1,638$ dofs regardless of the levels of local refinement used. The monotonic convergence in the enriched global strain energy is plotted in Fig. 12 corresponding to an h-extension performed in the local problem.

In this example problem the SIF extraction is performed using the contour integral method with the same extraction parameters used in both the GFEM^{gl} and hp-GFEM analyses [50]. The *hp-GFEM* model (as well as the local mesh in the GFEM^{gl} approach) is refined such that the ratio of the characteristic element size, l_e, to the half crack length, a, is approximately $\frac{l_e}{a} = 3 \times 10^{-2}$ for elements containing the crack front. This refinement guideline is taken from [51]. With this refinement level, we would expect the *GFEM* to deliver accurate results for a quasi-$2D$, through-thickness

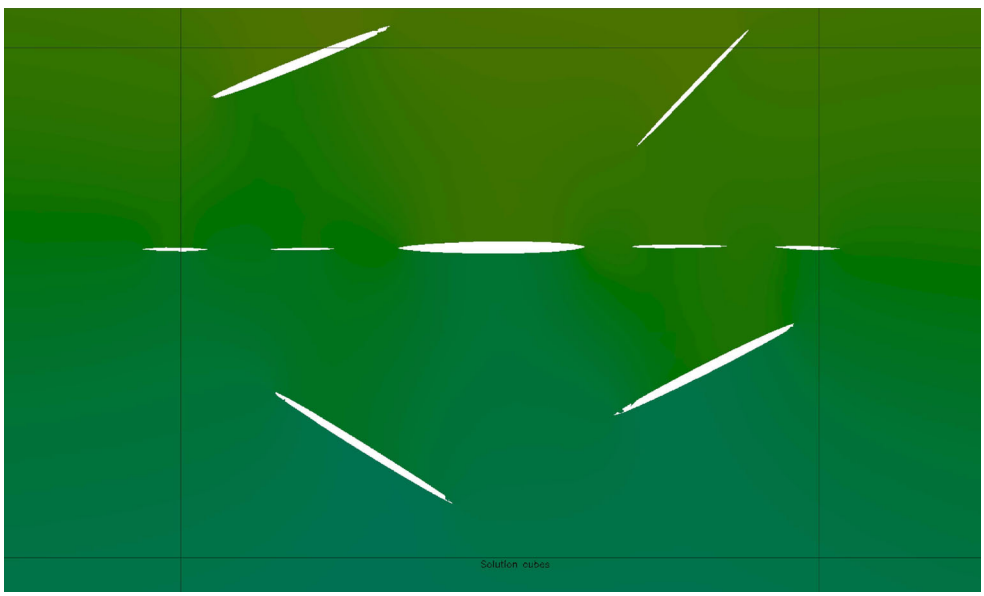

Fig. 11 Displacement contour generated with GFEM^{gl}. Note that there are nine discontinuity surfaces which are opened within one computational element. Displacement contour shown is scaled 5×

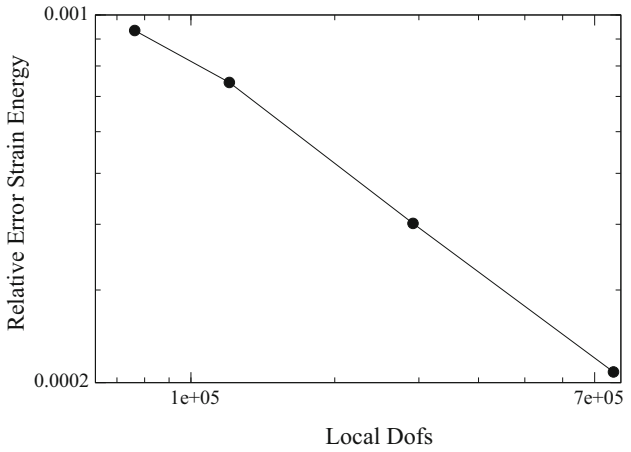

Fig. 12 Convergence in the enriched global strain energy for the multi-site damage model, corresponding to an h-extension in the local model

Table 3 Comparison of extracted K_I values at right crack front

Crack	GFEM^{gl}	hp-GFEM	Relative difference
1	60.513	61.164	0.0106
2	34.289	34.325	0.0010
3	36.794	36.433	0.0099
4	23.705	23.121	0.0253
5	33.878	32.964	0.0277
6	40.569	41.412	0.0204
7	26.253	25.468	0.0308
8	36.951	38.010	0.0279
9	46.396	47.674	0.0268

crack. The extracted SIF values are provided in Table 3 for both the GFEM^{gl} as well as hp-GFEM simulations. It can be seen from the table that the SIFs extracted with the GFEM^{gl} compare very well with those extracted using the hp-GFEM. In most cases the relative difference is in the neighborhood of 2–3 %.

Remark It should be noted that while propagation of the multiple crack surfaces is possible, the results would need to be interpreted very carefully. Essentially what needs to be considered is that each crack surface would have a different K_{eq}^{max} and thus care would need to be taken to ensure that the advancement of a particular crack vertex is scaled according to Eq. (11) to reflect the maximum overall K_{eq}^{max} and not merely the K_{eq}^{max} for each individual crack surface. Otherwise it cannot be ensured that each crack vertex in the overall model is subjected to the same number of loading cycles, and thus the results would be somewhat meaningless. This is merely a limitation of the current implementation, and not of the approach itself, and this type of analysis is considered beyond the scope of the present work. Focus on propagation/interaction of multiple crack surfaces utilizing a fixed, coarse (potentially hexahedral) finite element mesh is the topic of a subsequent paper.

Fig. 13 *GFEM*^{gl} model used for mixed-mode through-thickness crack propagation

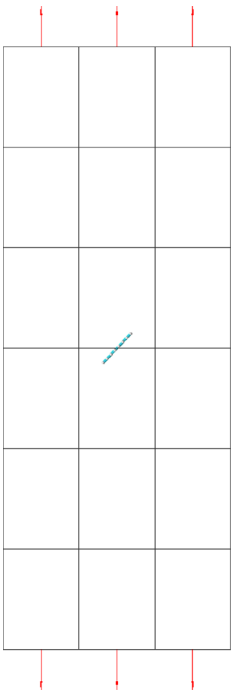

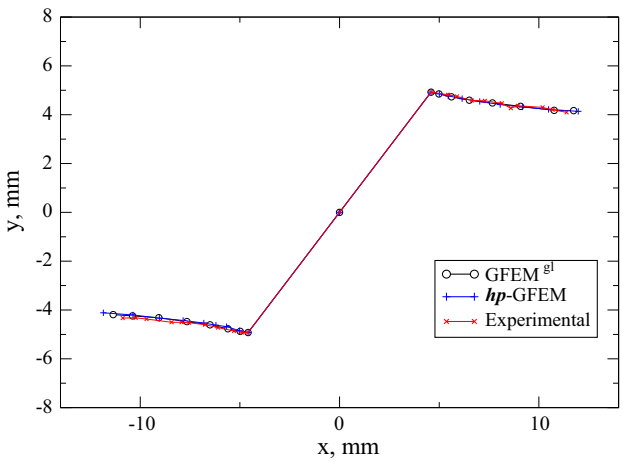

Fig. 14 Crack trajectory predicted both numerically and experimentally. The numerically computed crack path is in very good agreement with the experimentally obtained crack path

5.3 Mixed-mode through-thickness crack propagation

The example problem in this section illustrates the ability of the methodology to analyze the mixed-mode crack propagation of an inclined through-thickness crack, on a coarse hexahedral mesh. This includes the ability to represent a sharp crack kinking completely within one computational element, so as to avoid the use of an overly-refined, and therefore computationally inefficient FE mesh.

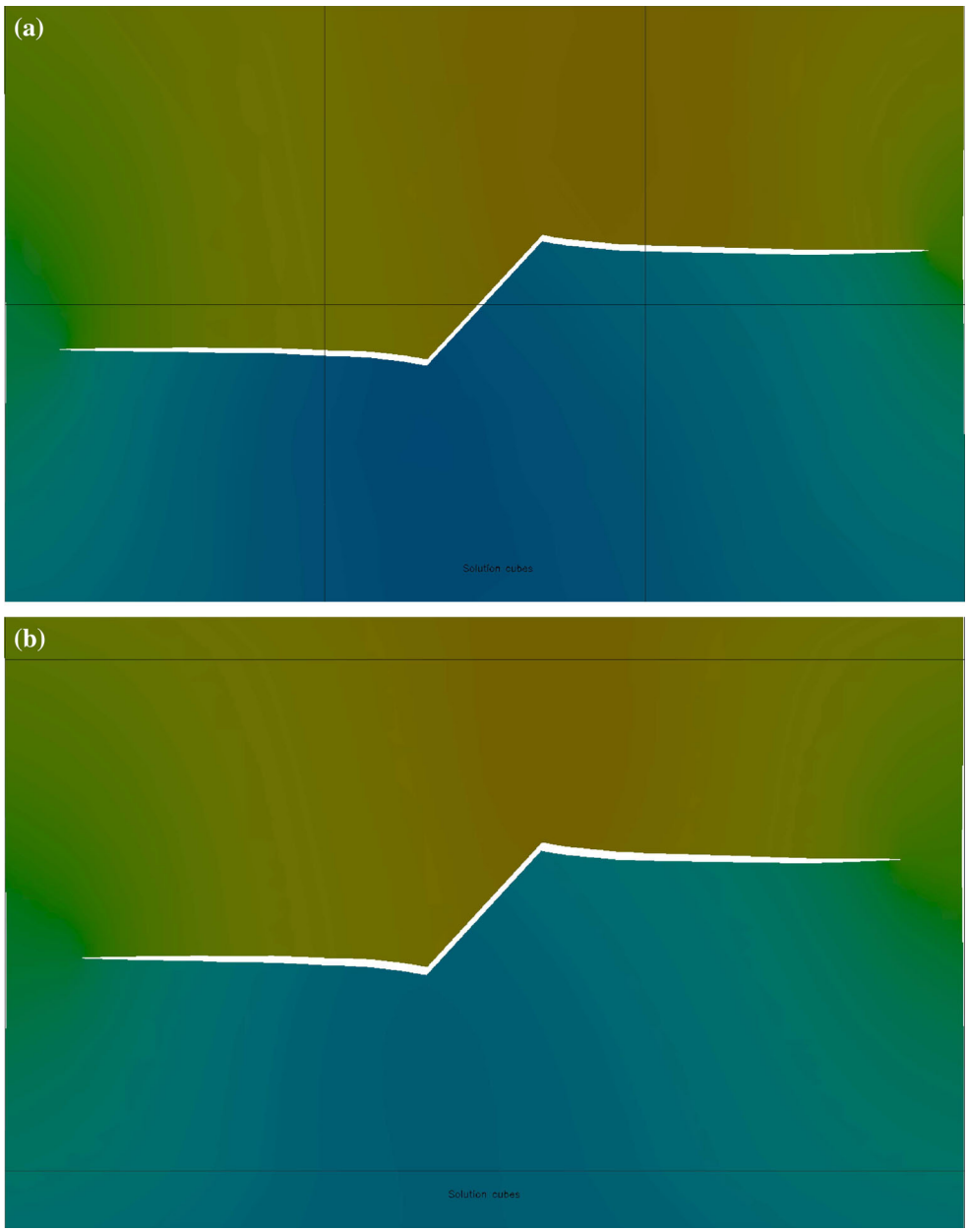

Fig. 15 Displacement contours generated with different global discretizations. Results are in very good agreement, and it may be noted that *solid black lines* indicate the actual computational elements used in the simulations. **a** Crack trajectory predicted with global model from Fig. 13. **b** Crack trajectory predicted with coarser global model

The domain has dimensions $(76.2 \times 203.2 \times 3.175)$ mm in the x-, y- and z-directions, respectively. The global model has $3, 6$ and 1 hexahedral elements in the x, y and z-directions, respectively. The domain is subjected to cyclic, normal tractions with maximum magnitude 172.37 MPa and $R = 0.1$, along the top and bottom faces, as indicated by the red arrows in Fig. 13. Young's Modulus is taken as $E = 115 \times 10^3 \frac{N}{mm^2}$ and Poisson's ratio is taken as, $\nu = 0.32$. The initial crack surface is inclined at an angle of 43° clockwise with respect to the y-axis. The initial crack surface has a total length of $2a = 13.46$ mm. Paris law parameters are taken as $C = 1.251 \times 10^{-11} \frac{mm}{cycle}$ and $m = 2.59$. In this particular problem, the SIFs are only extracted at the center crack front vertex, and each crack front vertex propagates the same distance/direction for a particular crack front stretch. This is done due both to the thin through-thickness dimension of the specimen as well as to allow for comparison against existing numerical results generated with hp-GFEM.

Results for the mixed-mode propagation simulation are presented in Fig. 14. There is data plotted corresponding to

the GFEM^{gl} results, results generated with hp-GFEM, as well as experimentally generated results from the literature [55]. Similar hp-GFEM results to those presented here can also be found elsewhere in the literature [52]. It can be seen from the plot that both the hp-GFEM as well as the GFEM^{gl} as presented in this paper, yield numerical results which compare very favorably with the experimental data, and the initial sharp kinking is accurately predicted.

A displacement contour computed using the GFEM^{gl} and the coarse global model shown in Fig. 13 is shown in Fig. 15a. In the figure, it should be noted that the solid black lines indicate the actual computational elements used to generate the displacement contour. It can be seen that the initial sharp kinking, commonly seen in mixed-mode crack propagation scenarios, can be well-represented entirely within one computational element entirely through the use of enrichment functions and the underlying explicit crack surface representation. This type of complex crack surface representation poses serious challenges on such a coarse mesh if using an implicit crack surface representation. Mesh objectivity of the predicted crack path in this case can be further illustrated with the use of an even coarser global discretization. A solution contour corresponding to a simulation run using a global mesh utilizing five elements in the y-direction and only one element in the x and z-directions, is shown in Fig. 15b. It can be seen from the figure that the predicted crack paths are in very good agreement with one another. In the latter case the entire propagated crack surface, including the two initial kinks, is still well represented and accurately predicted, even though the computational mesh has been coarsened.

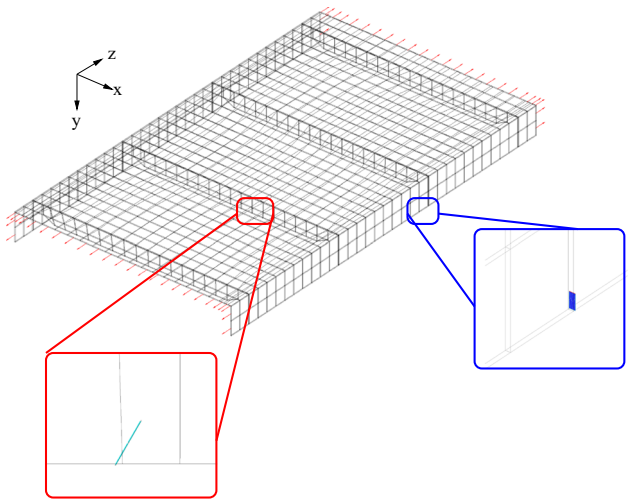

Fig. 16 Three-bay panel model, along with flange crack (*blue*) and stiffener crack (*red*) locations. *Red arrows* indicate traction boundary conditions applied in z-direction along front and back faces of the panel. (Color figure online)

5.4 Application to representative aerospace structure

In this section we simulate fatigue cracks propagating in a representative aerospace structure. The structure is a three-bay stiffened panel (Fig. 16) subjected to cyclic normal tractions with magnitude $10\,ksi$ applied in the z-direction. Material properties and Paris law parameters for a $Ti\,6242s$ alloy were obtained from [44], and taken as $E = 17,100\,ksi$, $\nu = 0.325$, $C = 1.17e^{-15}\frac{in}{cycle}$ and $m = 5.47$. The load ratio was taken as $R = 0.0$. The panel skin has dimensions ($19.6 \times 0.065 \times 34$) in the x-, y- and z-directions, respectively. There are two flanges located at $x = \pm 9.8$ with dimensions ($0.065 \times 2.5 \times 34$) in the x-, y- and z-directions, respectively. There are four stiffeners located at $z = \pm 5, \pm 10$ with dimensions ($17.6 \times 1.25 \times 0.065$) in the x-, y- and z-directions, respectively. The stiffeners taper linearly from a depth of 1.25 to 0.75 at each end, as can be seen in Fig. 17. All dimensions and locations reported in this section are in $inches$ and the origin is taken at the geometric center of the top surface of the panel. This panel-type structure is a good example of the type of structure that is easier to analyze with brick elements because it is easier to create a well-behaved coarse mesh than would be the case if global tetrahedral elements are used.

There are two crack locations investigated, which are illustrated in Fig. 16. The first crack is a thru-thickness flange crack with crack mouth located at $(x, y, z) = (9.8, 2.5, 3.0)$. The second crack is a thru-thickness stiffener crack with crack mouth located $(x, y, z) = (1.7, 1.25, -5.0)$. The stiffener crack location is selected based on the deflected shape of the stiffened panel when subjected to axial tension, as illustrated in Fig. 17, in which a tensile region develops in the lower portion of stiffener as the panel undergoes bending.

The first scenario considers both cracks separately, in Mode I configurations. That is to say that the crack surfaces are parallel with the global y-axis. It should be noted that the cracked configuration shown in the red box in Fig. 16 is in a mixed-mode configuration, which will be considered subsequently. Each crack has an initial length of $a_{cr} = 0.2$,

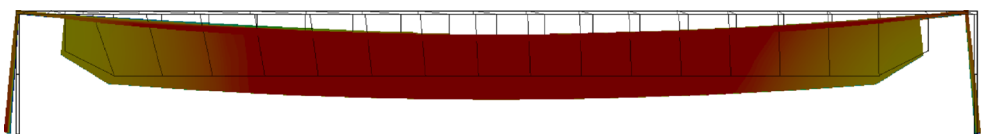

Fig. 17 Deflected shape of stiffened panel when subjected to axial tension

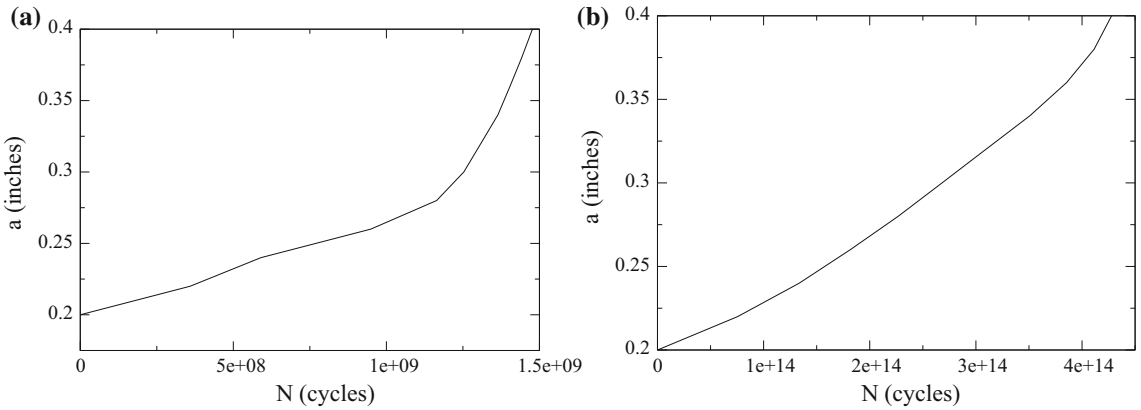

Fig. 18 Crack length versus loading cycles for flange crack (**a**) and stiffener crack (**b**). **a** Flange crack. **b** Stiffener crack

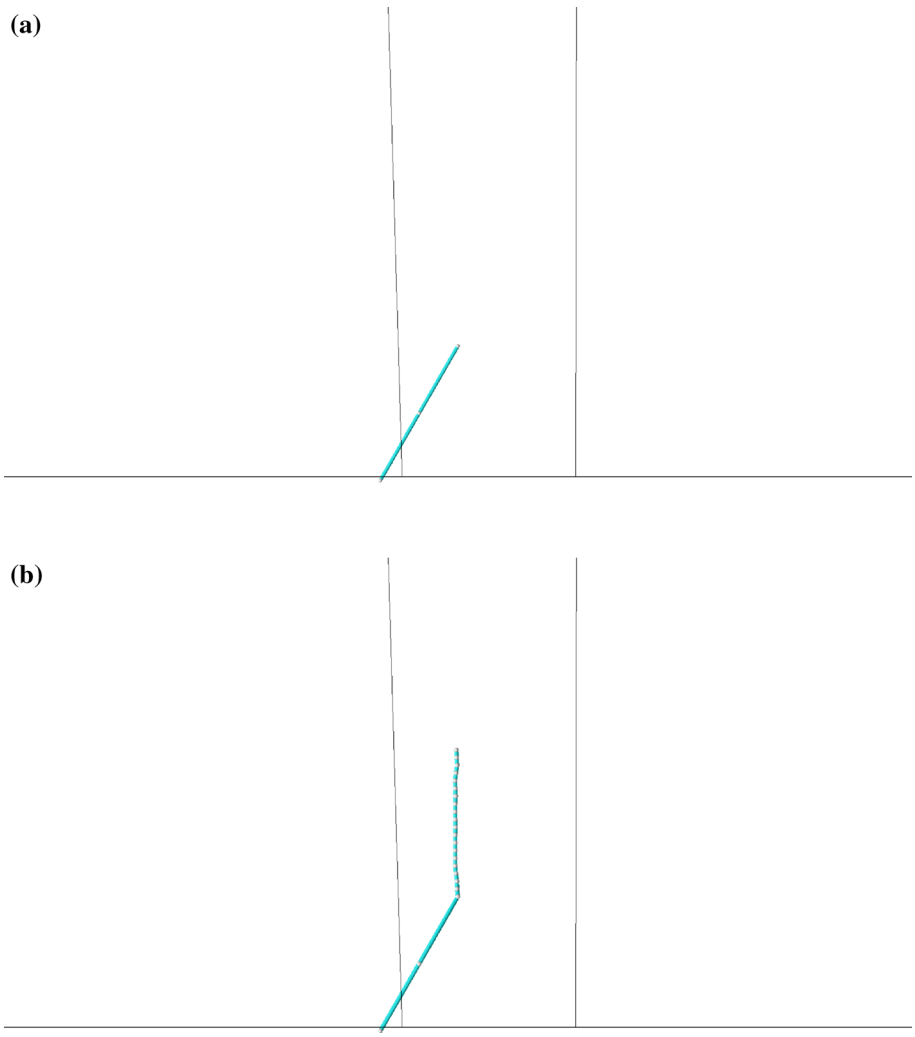

Fig. 19 Initial (**a**) and final (**b**) crack surfaces for mixed-mode crack propagation in panel stiffener. **a** Initial crack surface. **b** Final propagated crack surface

and simulations are run to compute the cycles necessary to grow the crack to twice its initial length, i.e. $a_{cr}^{final} = 0.4$. Similar to what is done in Sect. 5.3, the SIFs are only computed at the crack vertex in the center of the domain and each crack front is propagated uniformly. This is again due to the extremely thin thru-thickness dimension. The crack is propagated to twice its initial length in ten equal advancements, with $\Delta a_{max} = 0.02$, and cycle data is calculated via (10).

Figure 18 illustrates the crack length versus number of load cycles for each crack case investigated. As can be seen

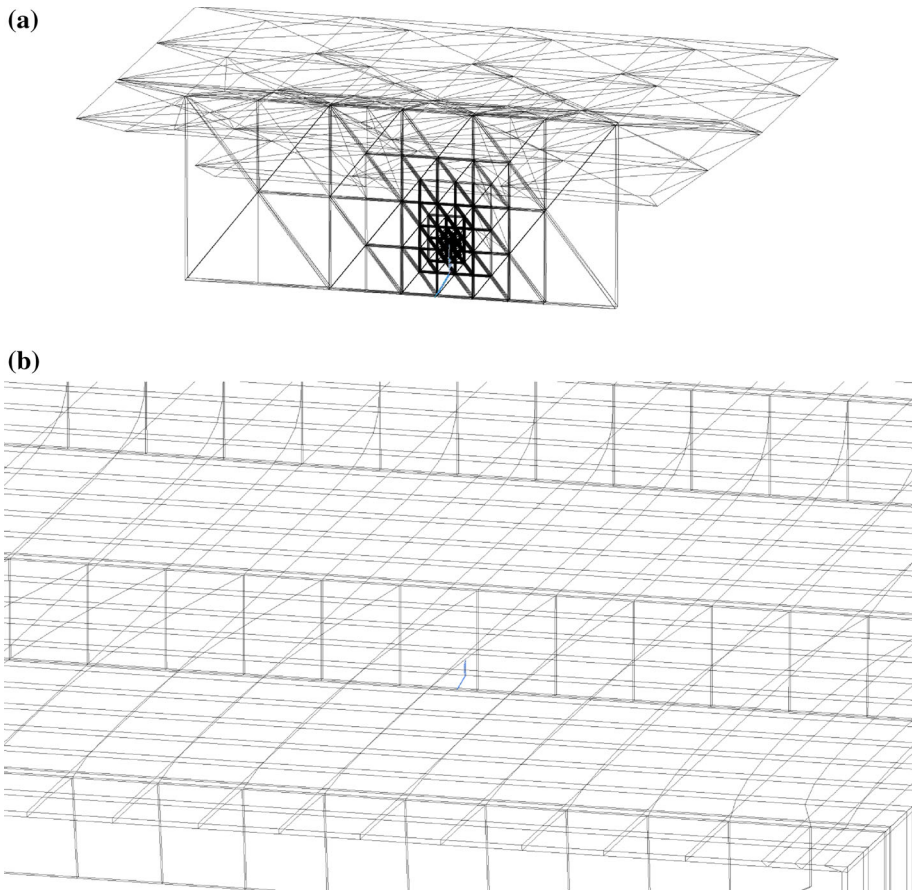

Fig. 20 Highly-adapted local (**a**), and coarse global discretizations (**b**) used to represent a propagated crack surface in a panel stiffener. **a** Local discretization. **b** Global discretization

in the figures, both cracks exhibit the same behavior with significant reduction in the number of load cycles for a given crack growth increment as the crack length, and therefore K_I value increase, as would be expected. It can also be seen that the the number of cycles required to double the length of the stiffener crack is essentially beyond the run-out for this particular loading case, and thus the flange crack is a much more critical flaw. This is not unexpected since the loading is transferred directly into the flange, whereas the loading in the stiffener is structural only, resulting from the out-of-plane bending exhibited as the stiffened panel itself is loaded axially.

Mixed-mode crack propagation The second case investigated is a mixed-mode stiffener crack, again with initial length $a_{cr} = 0.2$ propagated to twice its initial length. In this instance the crack is in a mixed-mode configuration, as seen in the red box in Fig. 16 as well as in Fig. 19a, in which the initial crack surface is rotated 30° clockwise with respect to the global y-axis, and with the crack mouth in the same location as in the Mode I configuration. As can be seen in Fig. 19b, the final crack shape indicates that again the crack orients itself in manner in which is it now normal to the maximum tensile stress, as would be expected.

The multi-scale nature of the approach is again illustrated in Fig. 20. The highly-adapted local domain is shown in Fig. 20a, where the *hp-GFEM* is used to accurately model the mixed-mode crack propagation, and the crack itself is then modeled in the coarse global model entirely through the use of the multi-scale enrichment functions, as shown in Fig. 20b.

6 Conclusions

This paper presents an extension of the GFEM^{gl} appropriate for fracture mechanics analyses on fixed, coarse hexahedral meshes. No explicit crack surface geometry engine appropriate for hexahedral elements is required as the crack surface is represented entirely through enrichment functions computed from a fine-scale model utilizing a tetrahedral mesh. As such, the *hp*-GFEM as presented in [51] can be used to model the crack only in the fine-scale problem and accurate representation in the coarse-scale model is accomplished entirely through the use of a multi-scale enrichment function. The approach allows for the extension of automated *hp*-adaptivity to hexahedral meshes and the associated ability to perform

accurate fracture analyses without any requirements of mesh irregularity or constrained approximations to retain C^0 continuity of the coarse-scale solution.

The proposed approach was successfully verified against *hp*-GFEM for two static crack benchmark problems: one simple Mode I problem and one fully mixed-mode example. The approach was also successfully verified against both *hp*-GFEM results as well as experimental data for a mixed-mode fatigue crack propagation scenario. The sharp initial kinking of the crack, a common occurrence in mixed-mode crack propagation problems, is accurately represented completely within *one* coarse, hexahedral element.

In addition to accurately modeling a sharp kinking in a crack surface, the proposed approach was able to accurately represent nine discrete discontinuity surfaces all opened within one hexahedral element. The approach was able to deliver very good accuracy when compared to the *hp*-GFEM approach with orders of magnitude reduction in the Dof requirements to accurately analyze the problem.

The final numerical example demonstrates the ability of the proposed approach to model crack propagation in a model of industrial complexity. Both Mode *I* and mixed-mode crack propagation simulation results are provided for cracks propagating in the flange and stiffener of a three-bay stiffened panel.

Acknowledgments The financial support of the Air Force Office of Scientific Research through Task No. 09RB07COR (Dr. David Stargel, Program Officer), is gratefully acknowledged.

References

1. Anderson TL (2005) Fracture mechanics: fundamentals and applications. CRC Press, Boca Raton
2. Arnold DN, Mukherjee A, Pouly L (2000) Locally adapted tetrahedral meshes using bisection. SIAM J Sci Comput 22(2):431–448
3. Babuška I, Melenk JM (1997) The partition of unity method. Int J Numer Methods Eng 40:727–758
4. Babuška I, Ihlenburg F, Paik E, Sauter S (1995) A generalized finite element method for solving the Helmholtz equation in two dimensions with minimal pollution. Comput Methods Appl Mech Eng 128(3–4):325–360
5. Bansch E (1991) Local mesh refinement in 2 and 3 dimensions. Impact Comput Sci Eng 3:181–191
6. Becker EB, Becker GF, Oden JT (1981) Finite elements: an introduction, vol 1., Texas finite element seriesPrentice-Hall, Englewood Cliffs
7. Belytschko T, Black T (1999) Elastic crack growth in finite elements with minimal remeshing. Int J Numer Methods Eng 45:601–620
8. Belytschko T, Fish J, Bayliss A (1990) The spectral overlay on finite elements for problems with high gradients. Comput Methods Appl Mech Eng 81:71–89
9. Belytschko T, Gracie R, Ventura G (2009) A review of extended/generalized finite element methods for material modeling. Model Simul Mater Sci Eng 17:24. doi:10.1088/0965-0393/17/4/043001
10. Costabel M, Dauge M, Yosibash Z (2004) A quasidual function method for extracting edge stress intensity functions. SIAM J Math Anal 35(5):1177–1202
11. Demkowicz L (2006) Computing with Hp-adaptive finite elements, vol 1., One and two dimensional elliptic and Maxwell problems Chapman & Hall/CRC, London
12. Demkowicz L, Oden JT, Rachowicz W, Hardy O (1989) Toward a universal h-p adaptive finite element strategy. Part 1. Constrained approximation and data structure. Comput Methods Appl Mech Eng 77:79–112
13. Dhatt G, Touzot G (1984) The finite element method displayed. Wiley, New York
14. Dompierre J, Labb P, Vallet M-G, Camarero R (1999) How to subdivide pyramids, prisms and hexahedra into tetrahedra. Rapport CERCA R99-78
15. Duarte CA, Babuška I (2002) Mesh-independent directional p-enrichment using the generalized finite element method. Int J Numer Methods Eng 55(12):1477–1492. doi:10.1002/nme.557
16. Duarte CA, Kim D-J (2008) Analysis and applications of a generalized finite element method with global-local enrichment functions. Comput Methods Appl Mech Eng 197(6–8):487–504. doi:10.1016/j.cma.2007.08.017
17. Duarte CA, Babuška I, Oden JT (2000) Generalized finite element methods for three dimensional structural mechanics problems. Comput Struct 77:215–232. doi:10.1016/S0045-7949(99)00211-4
18. Duarte CA, Hamzeh ON, Liszka TJ, Tworzydlo WW (2001) A generalized finite element method for the simulation of three-dimensional dynamic crack propagation. Comput Methods Appl Mech Eng 190(15–17):2227–2262. doi:10.1016/S0045-7825(00)00233-4
19. Duarte CAM, Oden JT (1995). Hp clouds–A meshless method to solve boundary-value problems. Technical Report 95-05, TICAM, The University of Texas at Austin, May 1995
20. Fish J (1992) The s-version of the finite element method. Comput Struct 43:539–547
21. Fish J, Nath A (1993) Adaptive and hierarchical modelling of fatigue crack propagation. Int J Numer Methods Eng 36:2825–2836
22. Fries T-P, Belytschko T (2010) The generalized/extended finite element method: an overview of the method and its applications. Int J Numer Methods Eng 84:253–304
23. Fries TP, Byfut A, Alizada A, Cheng KW, Schroder A (2011) Hanging nodes and xfem. Int J Numer Methods Eng 86:404–430
24. Garzon J, Duarte CA, Pereira JP (2013) Extraction of stress intensity factors for simulations of 3-D crack growth with the generalized finite element method. Key Eng Mater 560:1–36 (Special issue on Advances in Crack Growth Modelling)
25. Garzon J, O'Hara P, Duarte CA, Buttlar W (2014) Improvements of explicit crack surface representation and update within the generalized finite element method with application to three-dimensional crack coalescence. Int J Numer Methods Eng 97:231–273. doi:10.1002/nme.4573
26. Ghosh S, Raghavan P (2004) Multi-scale model for damage analysis in fiber reinforced composites with interfacial debonding materials. Int J Multiscale Comput Eng 2(4):621–645
27. Ghosh S, Lee K, Raghavan P (2001) A multi-level computational model for multi-scale analysis in composite and porous materials. Int J Solids Struct 38:2335–2385
28. Gupta V, Kim D-J, Duarte CA (2012a) Extensions of the two-scale generalized finite element method to nonlinear fracture problems. Int J Multiscale Comput Eng. Accepted for publication
29. Gupta V, Kim D-J, Duarte CA (2012) Analysis and improvements of global-local enrichments for the generalized finite element method. Comput Methods Appl Mech Eng 245–246:47–62. doi:10.1016/j.cma.2012.06.021

30. Holl M, Loehnert S, Wriggers P (2013) An adaptive multiscale method for crack propagation and crack coalescence. Int J Numer Methods Eng 93(1):23–51
31. Holl M, Rogge T, Loehnert S, Wriggers P, Rolfes R (2014) 3D multiscale crack propagation usingthe xfem applied to a gas turbine blade. Comput Mech 53:1
32. Hou TY, Wu X-H (1997) A multiscale finite element method for elliptic problems in composite materials and porous media. J Comput Phys 134:169–189
33. Kim D-J, Pereira JP, Duarte CA (2010) Analysis of three-dimensional fracture mechanics problems: a two-scale approach using coarse generalized FEM meshes. Int J Numer Methods Eng 81(3):335–365. doi:10.1002/nme.2690
34. Kim D-J, Duarte CA, Sobh NA (2011) Parallel simulations of three-dimensional cracks using the generalized finite element method. Comput Mech 47(3):265–282. doi:10.1007/s00466-010-0546-5
35. Kim D-J, Duarte C, Proenca S (2012) A generalized finite element method with global-local enrichment functions for confined plasticity problems. Comput Mech: 1–16. doi:10.1007/s00466-012-0689-7ISSN 0178-7675
36. Kim J, Duarte CA (2015) A new generalized finite element method for two-scale simulations of propagating cohesive fractures in 3-D. Int J Numer Methods Eng 181:189–208
37. Krause R, Rank E (2003) Multiscale computations with a combination of the h- and p-versions of the finite-element method. Comput Methods Appl Mech Eng 192:3959–3983
38. Lee S-H, Song J-H, Yoon Y-C, Zi G, Belytschko T (2004) Combined extended and superimposed finite element method for cracks. Int J Numer Methods Eng 59:1119–1136. doi:10.1002/nme.908
39. Li S, Mear ME, Xiao L (1998) Symmetric weak-form integral equation method for three-dimensional fracture analysis. Comput Methods Appl Mech Eng 151:435–459
40. Loehnert S, Belytschko T (2007) A multiscale projection method for macro/microcrack simulations. Int J Numer Methods Eng 71(12):1466–1482
41. Melenk JM (1995) On generalized finite element methods. PhD thesis, The University of Maryland
42. Melenk JM, Babuška I (1996) The partition of unity finite element method: basic theory and applications. Comput Methods Appl Mech Eng 139:289–314
43. Oden JT, Duarte CA, Zienkiewicz OC (1998) A new cloud-based hp finite element method. Comput Methods Appl Mech Eng 153:117–126. doi:10.1016/S0045-7825(97)00039-X
44. O'Hara P, Hollkamp J (2014) Modeling vibratory damage with reduced-order models and the generalized finite element method. J Sound Vib 333:6637–6650
45. O'Hara P, Duarte CA, Eason T (2009) Generalized finite element analysis of three-dimensional heat transfer problems exhibiting sharp thermal gradients. Comput Methods Appl Mech Eng 198(21–26):1857–1871. doi:10.1016/j.cma.2008.12.024
46. O'Hara P, Duarte CA, Eason T, Garzon J (2013) Efficient analysis of transient heat transfer problems exhibiting sharp thermal gradients. Comput Mech 51:743–764. doi:10.1007/s00466-012-0750-6
47. Oskay C (2011) A variational multiscale enrichment for modeling coupled mechano-diffusion problems. Int J Numer Methods Eng. doi:10.1002/nme.3258
48. Paris A, Erdogan F (1963) A critical analysis of crack propagation laws. J Basic Eng 85:528–534
49. Park K, Pereira JP, Duarte CA, Paulino GH (2009) Integration of singular enrichment functions in the generalized/extended finite element method for three-dimensional problems. Int J Numer Methods Eng 78(10):1220–1257. doi:10.1002/nme.2530
50. Pereira JP, Duarte CA (2005) Extraction of stress intensity factors from generalized finite element solutions. Eng Anal Bound Elem 29:397–413. doi:10.1016/j.enganabound.2004.09.007
51. Pereira JP, Duarte CA, Guoy D, Jiao X (2009) hp-Generalized FEM and crack surface representation for non-planar 3-D cracks. Int J Numer Methods Eng 77(5):601–633. doi:10.1002/nme.2419
52. Pereira JP, Duarte CA, Jiao X (2010) Three-dimensional crack growth with hp-generalized finite element and face offsetting methods. Comput Mech 46(3):431–453. doi:10.1007/s00466-010-0491-3
53. Pereira JP, Kim D-J, Duarte CA (2012) A two-scale approach for the analysis of propagating three-dimensional fractures. Comput Mech 49(1):99–121. doi:10.1007/s00466-011-0631-4
54. Plews JA, Duarte CA (2014) Bridging multiple structural scales with a generalized finite element method. Int J Numer Methods Eng. doi:10.1002/nme.4703
55. Pustejovsky MA (1979) Fatigue crack propagation in titanium under general in-plane loading. I Experiments. Eng Fract Mech 11:9–15
56. Rank E, Krause R (1997) A multi-scale finite element method. Comput Struct 64(1–4):139–144
57. Schöllmann M, Richard HA, Kullmer G, Fulland M (2002) A new criterion for the prediction of crack development in multiaxially loaded structures. Int J Fatigue 117:129–141
58. Simone A, Duarte CA, van der Giessen E (2006) A generalized finite element method for polycrystals with discontinuous grain boundaries. Int J Numer Methods Eng 67(8):1122–1145. doi:10.1002/nme.1658
59. Spievak LE, Wawrzynek PA, Ingraffea AR, Lewicki DG (2001) Simulating fatigue crack growth in spiral bevel gears. Eng Fract Mech 68:53–76
60. Strouboulis T, Copps K, Babuška I (2000) The generalized finite element method: an example of its implementation and illustration of its performance. Int J Numer Methods Eng 47(8):1401–1417
61. Strouboulis T, Copps K, Babuška I (2001) The generalized finite element method. Comput Methods Appl Mech Eng 190:4081–4193
62. Sukumar N, Moës N, Moran B, Belytschko T (2000) Extended finite element method for three-dimensional crack modelling. Int J Numer Methods Eng 48(11):1549–1570
63. Szabo BA, Babuška I (1988) Computation of the amplitude of stress singular terms for cracks and reentrant corners. In: Cruse TA (ed) Fracture mechanics: nineteenth symposium, ASTM STP 969, pp 101–124. Southwest Research Institute, San Antonio
64. Tada H, Paris P, Irwin G (2000) The stress analysis of cracks handbook, 3rd edn. ASME Press, New York
65. Turner DZ, Nakshatrala KB, Hjelmstad KD (2011) A stabilized formulation for the advection-diffusion equation using the generalized finite element method. Int J Numer Methods Fluids 66:64–81
66. Wawrzynek PA, Martha LF, Ingraffea AR (1988) A computational environment for the simulation of fracture processes in three-dimensions. In Rosakis AJ (ed) Analytical, numerical and experimental aspects of three dimensional fracture process, vol 91, pp 321–327. ASME AMD, ASME, New York
67. Yosibash Z (2012) Singularities in elliptic boundary value problems and elasticity and their connection with failure initiation. Springer, New York